

The dusty torus in the Circinus galaxy: a dense disk and the torus funnel^{★,★★}

Konrad R. W. Tristram¹, Leonard Burtscher², Walter Jaffe³, Klaus Meisenheimer⁴, Sebastian F. Hönig⁵,
Makoto Kishimoto¹, Marc Schartmann^{6,2}, and Gerd Weigelt¹

¹ Max-Planck-Institut für Radioastronomie, auf dem Hügel 69, 53121 Bonn, Germany
email: tristram@mpifr-bonn.mpg.de

² Max-Planck-Institut für extraterrestrische Physik, Postfach 1312, Gießenbachstraße, 85741 Garching, Germany

³ Leiden Observatory, Leiden University, Niels-Bohr-Weg 2, 2300 CA Leiden, The Netherlands

⁴ Max-Planck-Institut für Astronomie, Königstuhl 17, 69117 Heidelberg, Germany

⁵ Dark Cosmology Center, Niels Bohr Institute, University of Copenhagen, Juliane Maries Vej 30, 2100 Copenhagen, Denmark

⁶ Universitätssternwarte München, Scheinerstr. 1, 81679 München, Germany

Received 17 September 2013 / Accepted 26 November 2013

ABSTRACT

Context. With infrared interferometry it is possible to resolve the nuclear dust distributions that are commonly associated with the dusty torus in active galactic nuclei (AGN). The Circinus galaxy hosts the closest Seyfert 2 nucleus and previous interferometric observations have shown that its nuclear dust emission is particularly well resolved.

Aims. The aim of the present interferometric investigation is to better constrain the dust morphology in this active nucleus.

Methods. To this end, extensive new observations were carried out with the MID-infrared Interferometric instrument (MIDI) at the Very Large Telescope Interferometer, leading to a total of 152 correlated flux spectra and differential phases between 8 and 13 μm . To interpret this data, we used a model consisting of black-body emitters with a Gaussian brightness distribution and with dust extinction.

Results. The direct analysis of the data and the modelling confirm that the emission is distributed in two distinct components: a disk-like emission component with a size (FWHM) of $\sim 0.2 \times 1.1$ pc and an extended component with a size of $\sim 0.8 \times 1.9$ pc. The disk-like component is elongated along PA $\sim 46^\circ$ and oriented perpendicular to the ionisation cone and outflow. The extended component is responsible for 80% of the mid-infrared emission. It is elongated along PA $\sim 107^\circ$, which is roughly perpendicular to the disk component and thus in polar direction. It is interpreted as emission from the inner funnel of an extended dust distribution and shows a strong increase in the extinction towards the south-east. We find both emission components to be consistent with dust at $T \sim 300$ K, that is we find no evidence of an increase in the temperature of the dust towards the centre. From this we infer that most of the near-infrared emission probably comes from parsec scales as well. We further argue that the disk component alone is not sufficient to provide the necessary obscuration and collimation of the ionising radiation and outflow. The material responsible for this must instead be located on scales of ~ 1 pc, surrounding the disk. We associate this material with the dusty torus.

Conclusions. The clear separation of the dust emission into a disk-like emitter and a polar elongated source will require an adaptation of our current understanding of the dust emission in AGN. The lack of any evidence of an increase in the dust temperature towards the centre poses a challenge for the picture of a centrally heated dust distribution.

Key words. galaxies: active – galaxies: nuclei – galaxies: Seyfert – galaxies: individual: Circinus – galaxies: structure – techniques: interferometric

1. Introduction

Active galactic nuclei (AGN) are thought to play a major role in the formation and the evolution of galaxies. The AGN phase provides mechanisms for feedback from the supermassive black hole to its hosting galaxy and the intergalactic medium. Therefore, a thorough knowledge of the accretion process in AGN is required to understand their influence on the formation and evolution of galaxies. Especially little is known about the accretion process on parsec scales.

* Based on observations collected at the European Southern Observatory, Chile, programme numbers 073.A-9002(A), 060.A-9224(A), 074.B-0213(A/B), 075.B-0215(A), 077.B-0026(A), 081.B-0893(A), 081.B-0908(A/B), 383.B-0159(A), 383.B-0993(A), 087.B-0746(C), 087.B-0971(A-C), and 087.B-0266(H).

** Appendices are available in electronic form at <http://www.aanda.org>

A toroidal distribution of warm molecular gas and dust surrounding the central engine, the so-called *dusty torus*, is a key component of AGN. First of all, the torus plays an important role in fuelling the AGN activity: it either forms the passive reservoir of material for the accretion onto the supermassive black hole or, more intriguingly, it is itself the active driver of the accretion towards the black hole (Hopkins et al. 2012). Secondly, the dusty torus is held responsible for the orientation-dependent obscuration of the central engine (e.g. Antonucci 1993; Urry & Padovani 1995): when oriented face-on, a direct view of the central engine is possible through the cavity in the torus (Type 1 AGN); when oriented edge-on, the view towards the centre is blocked by the gas and dust of the torus (Type 2 AGN). This scenario is supported by multiple observational evidence, most importantly by the detection of broad emission lines in the polarised light of several Type 2 nuclei (e.g. Antonucci & Miller 1985; Lumsden et al. 2004), indicating that Type 2 sources host the same central

engine as Type 1 AGN. However, there is also a growing number of observations that challenge this simple picture, e.g. the discovery of true Type 2 sources (without broad emission lines in polarised light) and X-ray column densities discrepant with the optical classification (for a recent discussion of AGN obscuration, see e.g. [Bianchi et al. 2012](#)).

The dust in the torus is heated by the emission from the accretion disk. It re-emits this energy in the infrared ([Rees et al. 1969](#)): the innermost dust is close to its sublimation temperature and mainly emits in the near-infrared, while the dust at larger distances is at lower temperatures and emits in the mid-infrared ([Barvainis 1987](#)). Direct observations of the torus are thus best carried out at infrared wavelengths. However, the dust distributions are very compact: they are essentially unresolved by single-dish observations even with the largest currently available telescopes (e.g. [Horst et al. 2009](#); [Ramos Almeida et al. 2009](#)). Only by employing interferometric methods in the infrared is it possible to resolve the nuclear dust distributions in AGN.

To date, several interferometric studies of the nuclear dust distributions of individual galaxies have been carried out. In the Seyfert 2 galaxy NGC 1068, the interferometric observations reveal a hot, parsec-sized disk that is surrounded by warm dust extended in polar direction ([Wittkowski et al. 2004](#); [Jaffe et al. 2004](#); [Weigelt et al. 2004](#); [Poncet et al. 2006](#); [Raban et al. 2009](#)). A two-component structure was also found in the nucleus of the Circinus galaxy ([Tristram et al. 2007](#), see below). In NGC 424 (Sy 2) and NGC 3783 (Sy 1) the thermal dust emission appears extended along the polar axis of the system ([Beckert et al. 2008](#); [Hönig et al. 2012, 2013](#)). In NGC 4151, a Seyfert 1.5 galaxy, interferometric measurements in the near- and mid-infrared have provided evidence of both hot dust at the inner rim of the torus as well as warm dust farther out ([Swain et al. 2003](#); [Burtscher et al. 2009](#); [Kishimoto et al. 2009b](#); [Pott et al. 2010](#)). In the radio galaxy NGC 5128 (Centaurus A) on the other hand, only half of the mid-infrared emission appears to be of thermal origin ([Meisenheimer et al. 2007](#); [Burtscher et al. 2010](#); [Burtscher 2011](#)). Near-infrared reverberation measurements and interferometry of several Type 1 AGN have shown that the hot inner rim of the torus scales with the square root of the AGN luminosity ([Suganuma et al. 2006](#); [Kishimoto et al. 2011a](#)). Whether this is also true for the cooler dust in the body of the torus remains unclear after interferometric studies of small samples of galaxies in the mid-infrared ([Tristram et al. 2009](#); [Tristram & Schartmann 2011](#); [Kishimoto et al. 2011b](#)). Although a possible common radial structure for AGN tori has been proposed ([Kishimoto et al. 2009a](#)), the first study with a statistically significant sample of AGN shows a rather diverse picture of the dust distributions with quite large differences between the dust distributions in individual galaxies ([Burtscher et al. 2013](#)).

Because of computational limitations, initial radiative transfer calculations of geometrical torus models were carried out for smooth dust distributions (e.g. [Krolik & Begelman 1988](#); [Granato & Danese 1994](#); [Schartmann et al. 2005](#)). However, it was realised early on that the distribution of gas and dust is most likely clumpy ([Krolik & Begelman 1988](#)). For this reason, radiative transfer calculations of clumpy dust distributions have been carried out more recently (e.g. [Nenkova et al. 2002](#); [Schartmann et al. 2008](#); [Hönig & Kishimoto 2010](#)). First attempts to address the physics of the accreting nuclear material in AGN have been undertaken using hydrodynamical simulations ([Wada & Norman 2002](#); [Dorodnitsyn et al. 2008](#); [Schartmann et al. 2009](#); [Wada et al. 2009](#); [Wada 2012](#)). Nevertheless, the physical picture of the torus remains unclear. Most torus models were designed to correctly reproduce the infrared spectral energy distributions

(SEDs) of AGN and the silicate feature at $10\ \mu\text{m}$. Very little can be learned about the torus itself from such comparisons: very diverse models using different assumptions and parameters can produce similar SEDs ([Feltre et al. 2012](#)). The degeneracies in the SEDs can, at least partially, be broken by resolving the dust distributions. This is, as stated above, currently only possible with infrared interferometry.

At a distance of about 4 Mpc (1 arcsec \sim 20 pc, [Freeman et al. 1977](#)), the Circinus galaxy is the closest Seyfert 2 galaxy. It is the second brightest AGN in the mid-infrared (after NGC 1068) and, hence, a prime target for detailed studies of its nuclear distribution of gas and dust. The galaxy can be considered to be a prototypical Seyfert 2 galaxy with narrow emission lines ([Oliva et al. 1994](#)), broad emission lines in polarised light ([Oliva et al. 1998](#)), a prominent ionisation cone ([Veilleux & Bland-Hawthorn 1997](#); [Maiolino et al. 2000](#); [Wilson et al. 2000](#); [Prieto et al. 2004](#)), an outflow observed in CO ([Curran et al. 1998, 1999](#)), bipolar radio lobes ([Elmouttie et al. 1998](#)), a Compton thick nucleus and a reflection component in X-rays ([Matt et al. 1996](#); [Smith & Wilson 2001](#); [Soldi et al. 2005](#); [Yang et al. 2009](#)). The galaxy is inclined by $\sim 65^\circ$ and the nucleus is heavily obscured by dust lanes in the plane of the galaxy so that it is only visible longward of $\lambda = 1.6\ \mu\text{m}$ ([Prieto et al. 2004](#)).

A first set of interferometric measurements with the MID-infrared Interferometric instrument (MIDI) was presented in [Tristram et al. \(2007\)](#). The modelling of the interferometric data showed that an extended, almost round emission region with $T \lesssim 300\ \text{K}$ and a size of $\sim 2.0\ \text{pc}$ surrounds a highly elongated, only slightly warmer ($T \sim 330\ \text{K}$) emission region with a size of $\sim 0.4\ \text{pc}$. The latter component was found to have roughly the same orientation and size as a rotating molecular disk traced by H_2O masers ([Greenhill et al. 2003](#)). The observations were interpreted as a geometrically thick dust distribution with an embedded disk component. This “torus” was found to be oriented perpendicular to the ionisation cone and outflow. The fact that the model did not reproduce all details of the observations was attributed to a more complex dust distribution. However, the properties of the dust components were poorly constrained and no evidence of hot dust was found.

In this paper, new interferometric observations of the Circinus galaxy with MIDI in the mid-infrared are presented in order to shed more light on both the small scale structure of the dust distribution as well as on the properties of the extended dust component. The paper is organised as follows: the observations and data reduction are described in Sect. 2. The results are discussed in Sect. 3. The description of our modelling of the brightness distribution and the discussion of the torus properties are given in Sects. 4 and 5, respectively. A summary of the results is given in Sect. 6.

2. Observations and data reduction

2.1. Observations

The new interferometric observations of the Circinus galaxy with MIDI were carried out in April 2008 and 2009 as well as in April and May 2011. MIDI is the mid-infrared interferometer of the Very Large Telescope Interferometer (VLTI) on Cerro Paranal in northern Chile ([Leinert et al. 2003](#)). It combines the light of two telescopes and produces spectrally dispersed interferograms in the N -band between 8 and $13\ \mu\text{m}$. All observations of the Circinus galaxy were carried out in high sensitivity (HIGH_SENSE) mode and with the prism ($\lambda/\delta\lambda \approx 30$)

as the dispersive element. With a few exceptions, the calibrator stars HD 120404, HD 125687 and HD 150798 were observed with the Circinus galaxy. Other calibrators observed in the same night and with the same instrumental setup were only used to determine the uncertainties of the transfer function (see Sect. 2.2).

The primary quantities measured by MIDI are the correlated flux spectra $F_{\text{cor}}(\lambda)$ and the differential phases $\phi_{\text{diff}}(\lambda)$ (differential in wavelength, therefore also called “chromatic phases”) from the interferometric measurements, as well as the masked total flux spectra $F_{\text{tot}}(\lambda)$ from the single-dish measurements. F_{cor} and ϕ_{diff} contain information on the source morphology and depend on the baseline vector (projected baseline length BL and position angle PA), that is on the projected separation and orientation of the two telescopes. The visibilities $V(\lambda)$ commonly used in optical/IR interferometry are in principle obtained by $V(\lambda) = F_{\text{cor}}(\lambda)/F_{\text{tot}}(\lambda)$ (for details on the relation of the quantities for MIDI we refer to Tristram 2007). Each interferometric measurement determines one point of the Fourier transform of the brightness distribution of the source in the so-called uv plane. The actual point measured depends on the projected baseline of the interferometer, that is on BL and PA. The basic goal of interferometry is to sample the uv plane as completely as possible in order to draw inferences on the brightness distribution. To specifically probe the small scale structures and the more extended dust in the Circinus galaxy, the new observations were carried out mainly with two long baselines using pairs of the 8.2 m Unit Telescopes (UTs) as well as with the shortest baselines of the VLTI using the 1.8 m Auxiliary Telescopes (ATs).

Including the data from Tristram et al. (2007), the Circinus galaxy was observed in a total of 18 epochs between 2004 and 2011. A summary of the observation epochs, including observing date, baseline properties and the numbers of good and bad measurements, is given in Table 1. Figure 1 shows the measurements in the uv plane, colour coded according to their observing epoch. A detailed list of the individual measurements can be found in Table A.1 in Appendix A.

To increase the sampling of the uv plane and the observing efficiency in the new observations, we continuously observed the Circinus galaxy by directly repeating the interferometry and photometry exposures. In doing so, the time-consuming acquisition and setup procedures normally performed when changing sources with MIDI are omitted. Calibrators were observed at intervals of typically 1.5 h in order to determine the variations of the instrumental and atmospheric transfer function during the night and to estimate the calibration error (see Sect. 2.2). Using this observing method, an almost continuous measurement of the correlated fluxes can be obtained along a uv track, while the projected baseline vector moves through the uv plane due to the rotation of the Earth.

The large time span over which the observations were carried out leads to some inhomogeneity in the data. The instrumental capabilities and observing procedures evolved with time and both the UTs and ATs were used for the observations; differing integration times and chopping frequencies were used for the single-dish spectra; observations were carried out with different states of the adaptive optics and field stabilisation systems. The respective quantities and system settings are included in Table A.1 for each uv point. Any ramifications for the data resulting from these differences should be eliminated during the calibration process (see Sect. 2.2) because the calibrators were observed with the same set-up. For this reason, we combine all data into one data set in order to achieve the best possible uv coverage.

Table 1. List of the MIDI observation epochs for the Circinus galaxy.

Date	Baseline	BL [m]	PA [°]	Good	Bad
2004-02-12	U3-U2	43 to 43	19 to 21	2	0
2004-06-03	U3-U2	20 to 29	92 to 129	2	0
2005-02-21	U2-U4	87	35	0	1
2005-03-01	U3-U4	49 to 62	44 to 130	6	0
2005-04-18	U2-U4	89	60	1	0
2005-05-26	U2-U3	35 to 43	12 to 69	6	0
2006-05-18	U2-U3	23 to 31	84 to 114	4	0
2008-04-17	U1-U3	75 to 84	42 to 60	0	5
2008-04-18	U2-U4	76 to 89	33 to 156	26	2
2008-04-26	E0-G0	12 to 15	14 to 155	23	2
2009-04-15	U1-U3	54 to 92	8 to 90	17	1
2009-04-27	E0-G0	14 to 16	16 to 113	16	1
	H0-G0	24 to 25	138 to 164	3	1
2011-04-14	U1-U2	35	65	1	0
2011-04-17	U3-U4	47 to 62	33 to 124	10	0
2011-04-18	U2-U4	87 to 87	32 to 41	7	1
2011-04-19	U1-U3	86 to 86	35 to 37	2	0
2011-04-20	U2-U4	77 to 81	127 to 150	16	0
2011-05-06	C1-A1	14 to 15	26 to 104	10	1
	D0-B2	26 to 27	34 to 38	0	2
totals:				152	17

Notes. The table includes observing date, baseline parameters (telescope combination, range of baseline lengths and position angles) and number of (un)successful measurements. U in the baseline stands for Unit Telescope (UTs); A1 to H0 denote the stations of the Auxiliary Telescopes (ATs). Measurements were considered successful (“good”) if a fringe signal was tracked and sufficient signal was detected (see also Appendix A).

2.2. Data reduction

The data was reduced using the data reduction package EWS (Expert Work Station¹, Jaffe 2004) Version 2.0. Additional software² written in IDL was used to diagnose and analyse the data consistently. EWS implements the coherent integration method (e.g. Meisner et al. 2004) for the reduction of the interferometric data. In this method, the group delay and phase drifts caused by the atmosphere are determined from the data itself. Note that because of these drifts only the differential phases can be obtained with MIDI, not the “absolute” Fourier phases. After the group delay and phase drifts have been removed and the bad frames have been flagged, the interferometric signal is averaged coherently. Version 2.0 of EWS includes several improvements especially for the treatment of fainter sources (i.e. sources with correlated fluxes significantly below 1 Jy on the UTs, or 20 Jy on the ATs). For example, the group delay and water vapour phase estimation are significantly more robust and less biased than previously. A description of the improvements to the data reduction software can be found in Burtscher et al. (2012).

The parameter settings of EWS used to reduce the data of the Circinus galaxy are listed in Table 2. To extract the spectra, an optimised mask was determined for each observing epoch. The width of these masks scales with the width of the PSF and increases from 5.3 ± 1.5 pixels (0.45 arcsec for the UTs) at $8 \mu\text{m}$ to 7.4 ± 1.0 pixels (0.63 arcsec for the UTs) at $13 \mu\text{m}$. To reduce the total flux spectra, the bands for estimating the sky background were adjusted so that they are always located

¹ The software package “MIA+EWS” can be downloaded at: <http://home.strw.leidenuniv.nl/~jaffe/ews/index.html>

² This additional software is publicly available at: <http://www.blackholes.de/downloads.html>

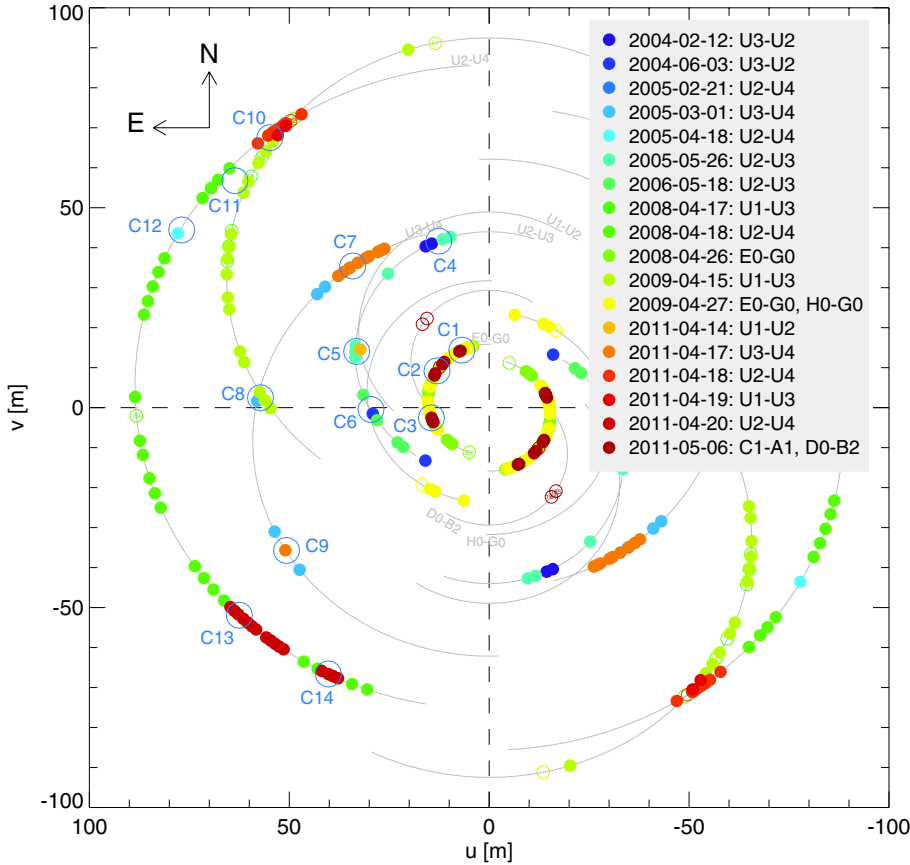


Fig. 1. uv plane with all MIDI measurements of the Circinus galaxy. The individual uv points are colour-coded according to the different observing epochs. Successful measurements are shown by filled circles, failed measurements by open circles. The full baseline tracks are plotted in grey for all the telescope combinations used and for a minimum elevation of the Circinus galaxy of 25° . In the baseline names, U stands for the UTs, A1 to G0 for the stations of the ATs. Regions used for the comparison of measurements at different epochs are encircled and labelled in blue (see Sect. 2.3). Every measurement appears twice, symmetric to the centre of the uv plane, because the Fourier transform of a real valued function (such as the intensity distribution on sky) is hermitian. As a consequence, the measurements which seem covered by the figure key are identical to those on the other side of the uv plane.

Table 2. Values for the parameters in EWS used for the reduction of the MIDI data of the Circinus galaxy.

Parameter	Value	Description
smooth	=10 frames	width of boxcar for high pass filtering
gsmooth1	=0.36 s	1st pass: coherent smoothing
asmooth1	=2.00 s	1st pass: amplitude smoothing ^a
msmooth1	=4.00 s	1st pass: median smoothing
gsmooth2	=0.36 s	2nd pass: coherent integration length
msmooth2	=1.00 s	2nd pass: median smoothing
ngrad	=2	2nd pass: 2 ngrad + 1 = 5 delay rate fits
maxopd1	=40 μm	2nd pass: maximum search OPD
psmooth	=0.18 s	smoothing for phase estimation
pgrad	=0	2 pgrad + 1 = 1 linear phase rate fit
maxopd2	=100 μm	flagging: maximum allowed OPD
minopd	=0 μm	flagging: minimum allowed OPD
jumpopd	=10 μm	flagging: maximum jump in delays
jitteropd	=1.5 μm	flagging: maximum jitter in delays

Notes. ^(a) Using a Gaussian instead of the default boxcar smoothing.

symmetric with respect to the source spectra, 15 or 16 pixels (~ 1.33 arcsec) apart for the UTs and 11 pixels (~ 4.2 arcsec) apart for the ATs. The calibrator database of EWS, which is based on the database of calibrator spectra by R. van Boekel (van Boekel 2004; Verhoelst 2005), was used to calibrate the data.

In addition to the statistical errors provided by EWS, the uncertainties due to the variation of the transfer function of the atmosphere and instrument were estimated from up to five calibrators and added to the statistical errors in quadrature. In most

cases, these calibration uncertainties dominate over the statistical errors. They are the main source of uncertainty in our MIDI measurements, with errors from as low as 5% to more than 20%, depending on the atmospheric conditions of the night. Similar results were obtained by e.g. Burtcher et al. (2012). The errors used in Tristram et al. (2007) are much smaller. There, only the statistical errors from EWS were used and the uncertainties were, therefore, underestimated.

Due to the imperfect background subtraction by chopping, the uncertainties in the total flux measurements are significantly larger than those of the correlated fluxes. These uncertainties also propagate into the visibilities. Furthermore, the total flux spectra of the Circinus galaxy observed with the ATs turn out to be entirely useless. Therefore most of the following analysis is focused on the correlated fluxes and the differential phases.

2.3. Data consistency

2.3.1. Individual points in the uv plane

Unless the brightness distribution of the object has changed in intensity or shape, MIDI should always measure the same correlated flux and differential phase at the same location in the uv plane. Furthermore, we expect measurements close in uv space to be similar or to change continuously for measurements at distances less than the telescope diameters of 8.2 m for the UTs and 1.8 m for the ATs (cf. López-Gonzaga et al. 2014).

For the Circinus galaxy, several locations in the uv plane have been measured more than once in different observing epochs or using different telescope combinations. For 14 such locations we check the consistency of our measurements. The locations are

Table 3. Comparison of measurements at similar locations in the uv plane but from different observing epochs or baselines.

#	A	B	$F_{\text{cor}}(\text{B})/F_{\text{cor}}(\text{A})$	$F_{\text{tot}}(\text{B})/F_{\text{tot}}(\text{A})$	$V(\text{B})/V(\text{A})$		
(1)	(2)	(3)	(4)	(5)	(6)		
C1	2008-04-26 00:55, E0-G0	2009-04-27 00:42, E0-G0	0.8 ± 0.3	–	–		
	2008-04-26 00:55, E0-G0	2011-05-06 00:25, C1-A1	0.9 ± 0.3	–	–		
	2009-04-27 00:42, E0-G0	2011-05-06 00:25, C1-A1	1.2 ± 0.3	–	–		
C2	2008-04-26 02:55, E0-G0	2009-04-27 02:52, E0-G0	0.8 ± 0.3	–	–		
	2008-04-26 02:55, E0-G0	2011-05-06 02:39, C1-A1	0.7 ± 0.3	–	–		
	2009-04-27 02:52, E0-G0	2011-05-06 02:39, C1-A1	0.8 ± 0.3	–	–		
C3	2008-04-26 06:31, E0-G0	2009-04-27 06:15, E0-G0	1.2 ± 0.3	–	–		
	2008-04-26 06:31, E0-G0	2011-05-06 05:48, C1-A1	0.9 ± 0.5	–	–		
	2009-04-27 06:15, E0-G0	2011-05-06 05:48, C1-A1	0.7 ± 0.4	–	–		
C4	2004-02-12 06:55, U3-U2	2005-05-26 23:29, U2-U3	1.9 ± 0.4	0.8 ± 0.6	b	2.5 ± 0.9	
C5	2005-05-27 04:07, U2-U3	2011-04-14 08:44, U1-U2	1.3 ± 0.2	1.1 ± 0.4	b	1.1 ± 0.3	
C6	2004-06-03 05:50, U3-U2	2006-05-18 06:16, U2-U3	1.0 ± 0.3	1.1 ± 0.4		0.9 ± 0.4	
C7	2005-03-01 04:06, U3-U4	2011-04-17 00:54, U3-U4	1.5 ± 0.3	b	–	–	
C8	2005-03-01 06:58, U3-U4	2009-04-15 09:29, U1-U3	1.1 ± 0.2	1.3 ± 0.6		0.9 ± 0.3	
C9	2005-03-01 09:21, U3-U4	2011-04-17 06:40, U3-U4	1.7 ± 0.2	b	1.2 ± 0.3	1.4 ± 0.2	b
C10	2009-04-15 05:16, U1-U3	2011-04-18 02:00, U2-U4	0.5 ± 0.3	r	0.6 ± 0.3	0.8 ± 0.4	r
	2009-04-15 05:16, U1-U3	2011-04-19 04:55, U1-U3	0.8 ± 0.3		0.9 ± 0.3	0.9 ± 0.4	
	2011-04-18 02:00, U2-U4	2011-04-19 04:55, U1-U3	1.4 ± 0.3	b	1.3 ± 0.4	1.0 ± 0.4	b
C11	2008-04-18 02:42, U2-U4	2009-04-15 06:00, U1-U3	1.2 ± 0.4	b	1.1 ± 0.3	1.0 ± 0.4	b
C12	2005-04-18 03:29, U2-U4	2008-04-18 02:59, U2-U4	1.5 ± 0.5	b	1.3 ± 0.5	1.2 ± 0.4	
C13	2008-04-18 08:18, U2-U4	2011-04-20 08:16, U2-U4	1.5 ± 0.3	b	–	–	
C14	2008-04-18 09:25, U2-U4	2011-04-20 09:28, U2-U4	1.5 ± 0.3	b	–	–	

Notes. Column 1 lists the identifiers of the comparison area (cf. blue numbers in Fig. 1); Cols. 2 and 3 list the time and baseline of the two measurements “A” and “B” that are compared; the ratios of the correlated flux spectra, the total flux spectra and the visibilities, averaged over the entire N -band, are given in Cols. 4–6 respectively. The ratio of the more recent measurement “B” over the earlier measurement “A” is calculated. Measurements which disagree by more than 1σ are highlighted in yellow, those that disagree by more than 2σ are highlighted in orange. If there is a change in the spectral shape, this is indicated by a “b” (more recent measurement is bluer) or “r” (more recent measurement is redder) after the corresponding value.

marked in blue in Fig. 1 and named C1 to C14. The ratios (averaged over the N -band) of the correlated flux spectra, the total flux spectra and the visibility spectra (where available) for the 22 possible comparisons at these locations are listed in Table 3. Also indicated is whether there is an apparent change in the spectral slope of the measurements: “b” indicates that the more recent measurement shows a bluer spectrum ($F_{\text{cor}}(13\mu\text{m})/F_{\text{cor}}(8\mu\text{m})$ decreased), “r” indicates that the more recent measurement shows a redder spectrum ($F_{\text{cor}}(13\mu\text{m})/F_{\text{cor}}(8\mu\text{m})$ increased).

For the correlated fluxes, 14 comparisons (i.e. 64%) agree within 1σ , and 20 (i.e. 91%) agree within 2σ . This is consistent with the statistical expectation and with the results for other sources, where measurements at approximately the same location in the uv plane have been repeated (e.g. NGC 424, NGC 3783 and NGC 4593, Hönl et al. 2012, 2013; Burtscher et al. 2013). Due to the larger errors in the total flux measurements, the total fluxes and visibilities all agree within 2σ . The differential phases all agree within 1σ , when taking into account the orientation of the baseline, because the sign of the differential phase switches for an interchange of the two telescopes, i.e. $\phi_{\text{diff}}(\text{U2-U1}) = -\phi_{\text{diff}}(\text{U1-U2})$. The total and correlated flux spectra, the visibilities and differential phases for C4, C5 and C6 are plotted in Fig. 2.

C4 has the strongest discrepancy: both the correlated flux and the visibility spectra measured in 2005 are about a factor of two higher than the ones measured in 2004 (see left column in Fig. 2). These early measurements were carried out without the VLTI infrared field-stabiliser IRIS (InfraRed Image Sensor,

Gitton et al. 2004). As a consequence, the beam overlap in the 2004 measurement was not optimal, which could be responsible for the lower correlated flux. In the case of C5 (middle column in Fig. 2), there is a slight increase in the correlated fluxes from 2005 to 2011. More interestingly, the (unusual) spectral shape with a dip at $12.5\mu\text{m}$ remains essentially unchanged. Therefore, we consider this feature to be a true signal from the source (see discussion in Sect. 5.2.3). In the case of C6 (right column in Fig. 2), one measurement obtained in 2004 lies between two measurements that were obtained in 2006. This is in perfect agreement with a continuous drop of the correlated fluxes or visibilities along this uv track.

For most of the comparisons (C4 to C14), the correlated fluxes measured at later epochs are higher than those measured earlier. This is especially the case at the short wavelength end of the N -band; the more recent spectra generally appear bluer. All of the observations showing this possible increase in flux were carried out with the UTs on baselines longer than 30 m, which essentially probe spatial scales of $\lesssim 80$ mas. Additionally, most of the total flux spectra observed since 2009 appear slightly (although not significantly) higher (see below). This could be interpreted as evidence of an increase in the source flux. On the other hand, the correlated fluxes obtained with the ATs, probing spatial scales of $\lesssim 170$ mas, rather suggest the opposite: the correlated fluxes observed in 2009 and 2011 are slightly lower than those observed in 2008 (cf. C1, C2 and C3 in Table 3). The decrease is not significant, but an overall increase in the flux on spatial scales below 170 mas can be ruled out.

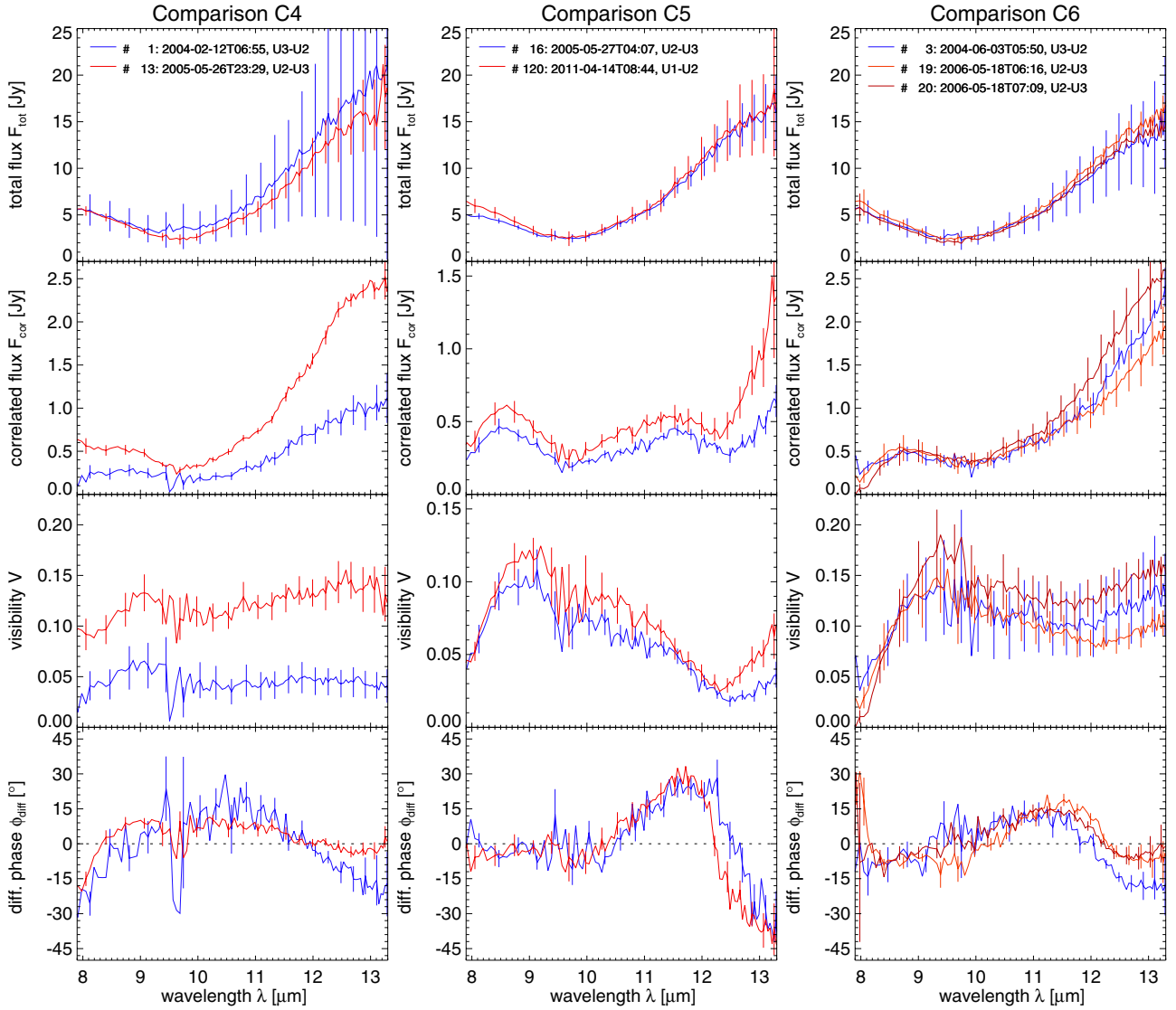


Fig. 2. Comparison of the total and correlated flux spectra (*first two rows*), visibilities (*third row*) and differential phases (*bottom row*) at locations C4 (*left column*), C5 (*central column*) and C6 (*right column*). For clarity, error bars are only plotted every fifth wavelength bin. Note that for C4 and C6 the telescopes at the two epochs considered were interchanged (UT3-UT2 versus UT2-UT3). The phases of measurements #1 and #3 were corrected for this interchange in order to allow an easier comparison (see also discussion in Sect. 5.2).

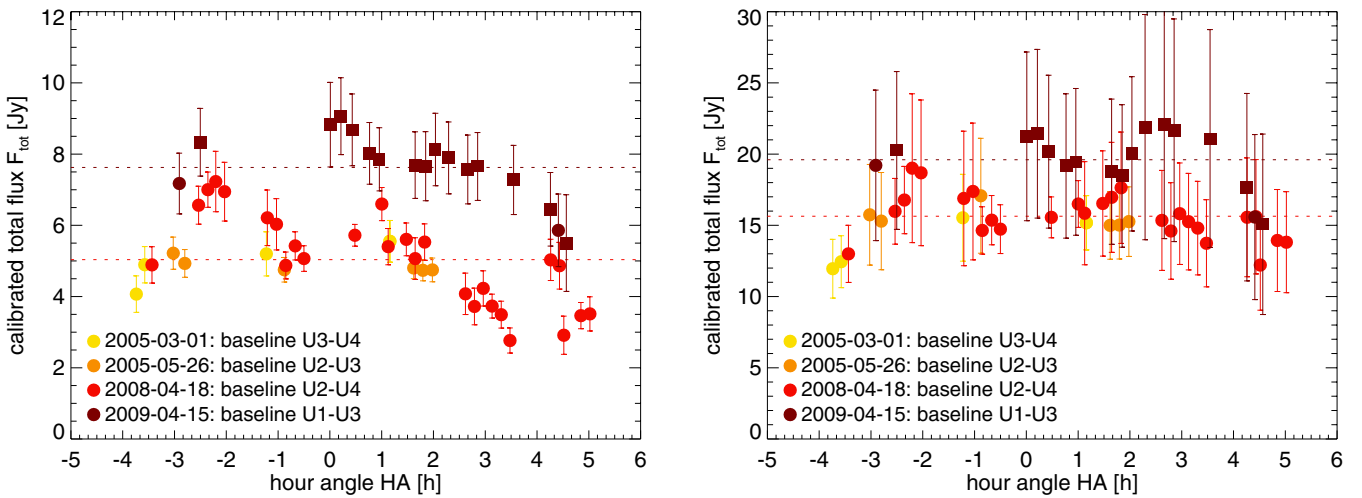


Fig. 3. Total flux of the Circinus galaxy at $8.2 \mu\text{m}$ (*left*) and $12.8 \mu\text{m}$ (*right*) as a function of the hour angle for four different epochs. The average fluxes at the respective wavelengths on 2008-04-18 and 2009-04-15 are indicated by the dashed lines.

2.3.2. Total flux

While there seem to be no significant discrepancies between the total flux spectra of the individual measurements, there are however clear trends when considering multiple measurements. In principle, MIDI should always measure the same calibrated total flux spectrum for a specific source, independent of the instrument settings and the baseline geometry. However, this is not the case for the Circinus galaxy, where significant changes in the total flux spectrum appear. Figure 3 shows the total fluxes at $8.2\ \mu\text{m}$ and $12.8\ \mu\text{m}$ as a function of the hour angle for four different epochs. In each of these epochs, the total flux spectrum was measured multiple times. The measurements obtained in 2005 are all consistent with each other. For the measurements obtained on 2008-04-18 and 2009-04-15, on the other hand, we find a clear decrease in the total flux with increasing hour angle at wavelengths shorter than $11.0\ \mu\text{m}$ (see left panel of Fig. 3): on 2008-04-18, the flux at $8.2\ \mu\text{m}$ apparently decreased from $\sim 7\ \text{Jy}$ at the start of the night to $\sim 3\ \text{Jy}$ at the end of the night, that is by more than a factor of two. At longer wavelengths, the flux levels remain more or less constant during the course of all of the observing runs (see right panel of Fig. 3). In addition, there seems to be a general increase in the total flux between 2008 and 2009. At $8.2\ \mu\text{m}$ the average flux (indicated by the dashed lines in Fig. 3) increased from $\sim 5.0\ \text{Jy}$ to about $7.6\ \text{Jy}$. At $12.8\ \mu\text{m}$ the increase is from $\sim 15.6\ \text{Jy}$ to $\sim 19.6\ \text{Jy}$.

We have carried out a thorough analysis to determine the cause for these changes in the total flux measurements. We checked if (1) possible changes in the instrumental setup; (2) the different airmasses of the observation; (3) variations of the atmospheric conditions; (4) changes in the performance of the adaptive optics system; or (5) variability of the calibrator could have caused the observed flux changes, but we find none of these explanations to be conclusive (for details, see Tristram 2013).

Slit losses might be responsible for the continuous flux decreases on 2008-04-18 and 2009-04-15. Especially before 2009, the Circinus nucleus was not always perfectly centred in the slit of MIDI due to an error in the reference position. For all our observations, the $200\ \mu\text{m}$ wide slit was used, corresponding to widths of $0.52\ \text{arcsec}$ and $2.29\ \text{arcsec}$ for the UTs and ATs respectively. Because the mid-infrared emission of the galaxy is slightly extended already in single-dish observations (e.g. Packham et al. 2005) and the field of view of MIDI rotates on the sky over the course of a night, this could have lead to a gradual decrease in the measured total fluxes. On the other hand, the resolved emission constitutes only about 20% of the total N -band emission of the Circinus nucleus (Packham et al. 2005; Reunanen et al. 2010). By consequence, slit losses due to the orientation of the extended emission cannot account for a change of the flux by up to a factor of two. Furthermore, it is unclear why such slit losses should not have played a role in 2005 and why they should only have an effect at short wavelengths, where potential slit losses should instead be reduced. A more accurate positioning of the source in the slit in 2009 could also explain the increase in the total flux for these measurements. The effect is, however, not sufficient to explain all of the observed increase.

If the light of the Circinus galaxy were significantly polarised, the rotation of the field of view together with the MIDI and VLTI optics could lead to a smooth change of the flux over the night. To obtain the observed change by a factor of 2 at $8.2\ \mu\text{m}$ on 2008-04-18, this would require a degree of polarisation of 50% at the short wavelength end of the N -band. There are no polarisation measurements for the Circinus galaxy in the N -band, but in the K -band the nucleus of the Circinus galaxy has

a polarisation of the order of 3 to 4% (Alexander et al. 2000). The degree of polarisation of NGC 1068 in the mid-infrared is less than 3% (Smith et al. 2000; Packham et al. 2007), that of Mrk 231, a Seyfert 1 galaxy, 8% (Siebenmorgen & Efstathiou 2001). It therefore seems unlikely that the mid-infrared emission of the nucleus of the Circinus galaxy is much higher polarised and that the degree of polarisation is strongly wavelength dependent.

A further possible explanation is that the emission from the Circinus galaxy itself has changed. As the mid-infrared emission is dominated by the emission from warm dust, variations on timescales of hours are not plausible and cannot be held responsible for the flux decrease observed in the course of a night. An increase in the flux over the period of one year, on the other hand, is very well possible physically. Indeed there is further evidence that the total flux of the Circinus galaxy has increased intrinsically between 2008 and 2009: a flux increase is also seen in single-dish photometry at $11.9\ \mu\text{m}$ with VISIR and the acquisition images obtained with MIDI. There are, however, also inconsistencies with an increase in the intrinsic mid-infrared flux of the nucleus of the Circinus galaxy. Because the increase took place over a period of less than a year, the variable emission should come from a region smaller than $1\ \text{ly} \approx 0.3\ \text{pc}$, i.e. $15\ \text{mas}$ on the sky. Therefore the increase in the flux should be mainly seen in the correlated fluxes on longer baselines, which probe exactly these spatial scales. Although there seems to be a slight increase in the correlated flux measurements since 2009, it is only by a few hundred mJy (see previous Sect.). This is by far not enough to explain the increase in the total flux by more than 2 Jy. Furthermore, the AT measurements do not show an increase in the correlated fluxes but rather a decrease. In summary this means we have (1) a flux *increase* by up to a few hundred mJy within $\sim 80\ \text{mas}$; (2) a possible flux *decrease* within $\sim 170\ \text{mas}$; and (3) an *increase* by more than 2 Jy within $\sim 500\ \text{mas}$. This is hard to explain physically. At least two “bursts” would have to be travelling outward through the dust distribution.

So far, no studies of the infrared variability of the Circinus galaxy have been published. Therefore, we started a more detailed investigation ourselves, including monitoring observations. A detailed discussion of the variability in the nucleus of the Circinus galaxy goes beyond the scope of this paper and will be presented in a future publication.

2.3.3. Conclusion from the data consistency checks

We conclude that the differences between the individual measurements of the correlated fluxes at the same position in the uv plane are in general consistent with the statistical expectations. On the other hand, there is no clear picture that can explain (1) the continuous decrease in the total flux during the observations on 2008-04-18 and 2009-04-15 as well as (2) the increase in the total flux between 2008 and 2009. For the following analysis, we will simply assume that the emission intrinsic to the Circinus galaxy has not changed between the interferometric measurements. We base this assumption on the fact that the correlated fluxes on the shortest baseline, i.e. within spatial scales of $\sim 170\ \text{mas}$ essentially remained constant. Because our further analysis and modelling is mainly based on the correlated fluxes and the differential phases, we are confident that the general results do not depend on a full discussion of possible variability. Furthermore, we find no solid basis on which to reject individual measurements that do not agree with other measurements. Therefore, we will retain all measured uv points for the following analysis.

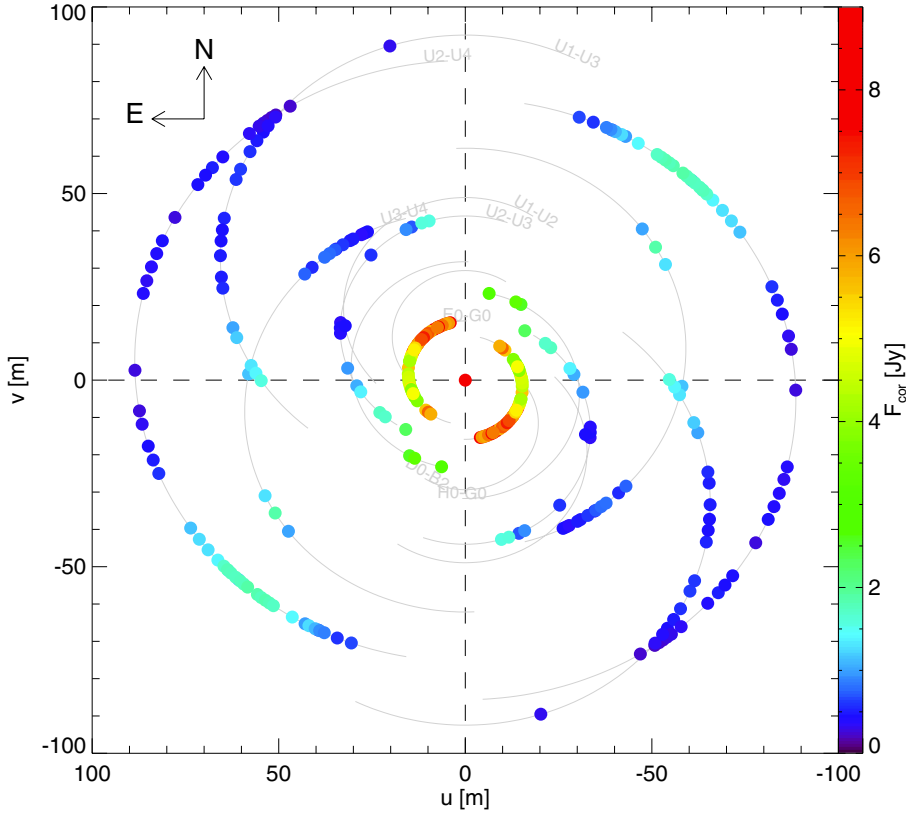


Fig. 4. Correlated fluxes of the Circinus galaxy at $12\ \mu\text{m}$ for all uv points containing useful interferometric data. The points are colour-coded according to their correlated flux, $F_{\text{cor}}(12\ \mu\text{m})$, using a square root colour scaling as indicated in the colour bar on the right. The uv point at the origin represents the averaged total flux of the source, which is outside the plotted range of colours: $\overline{F}_{\text{tot}}(12\ \mu\text{m}) = 10.7\ \text{Jy}$.

3. Results

In total we obtained 152 useful measurements of the correlated flux spectra and differential phases and 74 useful measurements of the total flux spectra. This includes 20 correlated flux measurements already published in [Tristram et al. \(2007\)](#).

The new reduction of the previously published data in general increases the data quality. The positive bias of the correlated fluxes and visibilities in the ozone feature between 9.5 and $10.0\ \mu\text{m}$ and at the edges of the N -band is reduced, especially for the data observed in 2004 and 2005. The more accurate group delay estimation leads to a slight increase in the correlated fluxes at the long wavelength end, but the overall spectral shape and flux levels remain unchanged. With correlated flux levels of more than $0.4\ \text{Jy}$ at $12.0\ \mu\text{m}$ in most cases, the result is robust with respect to the data reduction, and we obtain no contradictions to the values published in 2007. Due to the improved masking and sky residual estimation, the scatter of the total flux spectra is reduced significantly. The wavelength calibration of the MIDI spectra in EWS was also corrected slightly, resulting in a shift of the spectra to shorter wavelengths by about $0.1\ \mu\text{m}$. All spectra were corrected for the peculiar redshift of the Circinus galaxy of $z = 0.00145$ ($v_{\text{sys}} = 434 \pm 3\ \text{km s}^{-1}$, [Koribalski et al. 2004](#)).

All 74 useful measurements of the total flux spectra were combined by a weighted average to obtain a single estimate for the total flux spectrum of the Circinus nucleus: $\overline{F}_{\text{tot}}$. The spectrum agrees with the one published in 2007. It is shown as part of Fig. 10. The spectrum rises from $\sim 6\ \text{Jy}$ at $8\ \mu\text{m}$ to $\sim 16\ \text{Jy}$ at $13\ \mu\text{m}$, which is quite “red” ($\overline{F}_{\text{tot}}(8\ \mu\text{m}) < \overline{F}_{\text{tot}}(13\ \mu\text{m})$) and indicative of emission from warm ($T \sim 290\ \text{K}$) dust. The spectrum is dominated by a deep silicate absorption feature over almost the entire N -band. For the following, we will consider the total

flux spectrum as a measurement with a projected baseline length of $\text{BL} = 0\ \text{m}$.

We use all measurements of the correlated fluxes and phases individually and do not average measurements close in uv space. All useful correlated fluxes at $12\ \mu\text{m}$ are listed in Table A.1 and plotted in Fig. 4. With correlated fluxes at $12\ \mu\text{m}$ ranging from $\sim 8\ \text{Jy}$ (corresponding to $V \sim 0.8$) on the shortest baselines to $\sim 0.4\ \text{Jy}$ ($V \sim 0.04$) on certain long baselines, we clearly resolve the mid-infrared emission in the nucleus of the Circinus galaxy. The uv plane also shows that along certain position angles, the correlated flux is higher than along others. A very prominent example is the increase at the end of the baseline UT2-UT4, leading to cyan and green colours (corresponding to $F_{\text{cor}}(12\ \mu\text{m}) > 1.5\ \text{Jy}$) in Fig. 4. This increase will be discussed in Sect. 3.2.

Many of the correlated flux spectra (see Fig. A.1 in the appendix) have a shape similar to the total flux spectrum. Especially on short baselines, the correlated flux spectra are similar to the total flux spectrum when the spectral change due to the resolution effect at different wavelengths is taken into account.

On longer baselines, however, this is not always the case. Most noticeably, the short wavelength emission often either disappears completely or there is a downturn in the correlated flux shortward of $8.7\ \mu\text{m}$ without any significant signal in the differential phases (see e.g. C6 in Fig. 2). Interestingly, a similar decrease, albeit mainly in the visibilities and for $\lambda < 9.0\ \mu\text{m}$, might also be present in certain uv points for NGC 424 ([Hönig et al. 2012](#)) and NGC 3783 ([Hönig et al. 2013](#)). Contamination of the total flux by the wings of a spatially extended polycyclic aromatic hydrocarbon (PAH) feature at $7.7\ \mu\text{m}$ was discussed as a possible reason in [Hönig et al. \(2012\)](#). This would, however, only affect the visibilities and not the correlated fluxes we are considering here. Furthermore, the 8.6 and $11.3\ \mu\text{m}$ PAH features are

completely absent in our MIDI total flux spectrum (see inset of Fig. 10) or the nuclear spectra obtained by Roche et al. (2006)³. Because the $7.7\ \mu\text{m}$ feature is roughly correlated to the $8.6\ \mu\text{m}$ feature (Galliano et al. 2008) and, in AGN environments, suppressed with respect to the $11.7\ \mu\text{m}$ feature (Smith et al. 2007), we conclude that any contribution from the wing of the $7.7\ \mu\text{m}$ feature to our nuclear fluxes is negligible. For these reasons we rule out any PAH contamination to be responsible for the downturn of the correlated flux shortward of $8.7\ \mu\text{m}$. A further possible explanation could be instrumental/calibration effects, especially correlation losses (Burtscher et al. 2012). However, this would not explain why the downturn appears so abruptly for $\lambda < 8.7\ \mu\text{m}$. The correlation losses should instead be a smooth function of wavelength and only become significant for $F_{\text{cor}}(12\ \mu\text{m}) < 150\ \text{mJy}$ (Burtscher et al. 2013). This is not the case for the measurements at hand. It seems that the emission at the shortest wavelengths is almost fully resolved out and thus comes from an extended emission region (see discussion in Sect. 5.4).

In a few measurements, also a decrease in the correlated fluxes at longer wavelengths is present (see e.g. C5 in Fig. 2). In these cases, strong gradients in the differential phases also appear. We interpret these signatures (which are also present in the visibilities) as evidence of a more complex brightness distribution with small scale structure (see discussion in Sect. 5.2.3).

3.1. Radial dependency of the correlated fluxes

The correlated fluxes (and visibilities) at $12\ \mu\text{m}$ as a function of the projected baseline length BL are shown in Fig. 5. The correlated fluxes quickly drop from the total flux of $10.7\ \text{Jy}$ to less than $2\ \text{Jy}$ ($V \lesssim 20\%$) at $\text{BL} \sim 30\ \text{m}$. On longer baselines, the correlated fluxes remain on more or less the same level between $0.2\ \text{Jy}$ and $2.0\ \text{Jy}$. Note that the apparent scatter in the measurements at a certain baseline length is mainly due to measurements at different position angles (see next section).

The rapid drop at short baseline lengths implies that the mid-infrared emission is mostly resolved out by the interferometer. More precisely, only about 20% of the mid-infrared emission comes from structures smaller than about 70 mas in diameter. 80% of the emission is located on spatial scales between $\sim 70\ \text{mas}$ and $\sim 500\ \text{mas}$. The new observations with the ATs (at baseline lengths of $\text{BL} \sim 15\ \text{m}$) now also probe the majority of the flux in this extended emission region.

Because the correlated fluxes do not decrease much farther for $30\ \text{m} \lesssim \text{BL} \lesssim 95\ \text{m}$ (a change of the baseline length and, thus, spatial resolution by a factor of three), a single or several unresolved structures (“clumps”) with sizes below the resolution limit of the interferometer of about 15 mas must be present. The two regimes of the visibility function suggest that the corresponding brightness distribution has two distinct spatial scales: a large scale that is quickly resolved by the interferometer when increasing the baseline length and a small scale that essentially remains unresolved even at the longest baselines (i.e. at the smallest spatial scales probed by the interferometer).

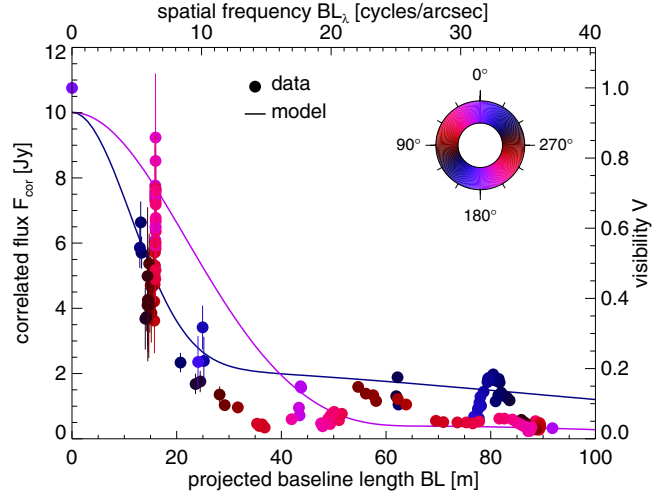


Fig. 5. Correlated fluxes (F_{cor} , left ordinate) or visibilities ($V = F_{\text{cor}}/\overline{F}_{\text{tot}}$, right ordinate) of the Circinus galaxy at $12\ \mu\text{m}$ as a function of the projected baseline length BL (bottom axis) or spatial frequency (top axis). The data are colour-coded with the position angle (see compass on the top right). Overplotted by two thick continuous lines are the correlated fluxes of the three-component model discussed in Sect. 4. The correlated fluxes of the model are along $\text{PA} = 17^\circ$ (violet) and $\text{PA} = 137^\circ$ (dark blue). Note that the errors in the measurements with UT baselines ($\text{BL} > 30\ \text{m}$) are smaller than the plot symbol and that the model does not fully reproduce the total flux (plotted at $\text{BL} = 0\ \text{m}$) for $\lambda > 11.5\ \mu\text{m}$ (see Sect. 5.3).

3.2. Angular dependency of the correlated fluxes

There are two telescope combinations, E0-G0⁴ (using the ATs) and UT2-UT4 (using the UTs), where the projected baseline lengths roughly remain the same while the position angle changes over a wide range due to the rotation of the Earth. This means the same spatial scales are probed in different directions. The correlated fluxes can therefore be directly compared to infer information on the source size in different directions under the assumption of a smooth, centrally peaked brightness distribution. The correlated fluxes at 8.5 and $12.0\ \mu\text{m}$ for the two mentioned baselines are shown in Fig. 6 as a function of the position angle. On both baselines and at both wavelengths, a clear dependency of the correlated fluxes on the position angle is present.

With the E0-G0 baseline, $13\ \text{m} < \text{BL} < 16\ \text{m}$, spatial scales of the order of 150 mas are probed. The uncertainties and scatter in the data points are relatively large because these measurements were obtained with the ATs. Nevertheless, the correlated fluxes show a clear trend with a broad minimum at $\text{PA} \sim 90^\circ$ at both 8.5 and $12.0\ \mu\text{m}$. This essentially means that the emission is better resolved in this direction, i.e. it is more extended along this position angle.

The UT2-UT4 baseline has projected baseline lengths between $76\ \text{m}$ and $90\ \text{m}$, corresponding to spatial scales of about 25 mas. The correlated fluxes show a very pronounced peak at $\text{PA} \sim 135^\circ$ with correlated fluxes more than three times higher than at other position angles. This means that the source appears significantly less resolved in this direction, while it is better resolved in all other directions. Such a dependency on the position angle can be explained by an extremely elongated emission component. Furthermore there is a second, much weaker peak at $\text{PA} \sim 60^\circ$ in the correlated fluxes at $12.0\ \mu\text{m}$. This peak

³ On scales of tens of arcseconds ($>200\ \text{pc}$) however, the Circinus galaxy indeed shows significant PAH emission at 7.7 , 8.6 and $11.3\ \mu\text{m}$ (Moorwood et al. 1996; Galliano et al. 2008), most likely from the circumnuclear starburst.

⁴ This telescope combination is identical to the combination C1-A1 measured in 2011 modulo an interchange of the telescopes.

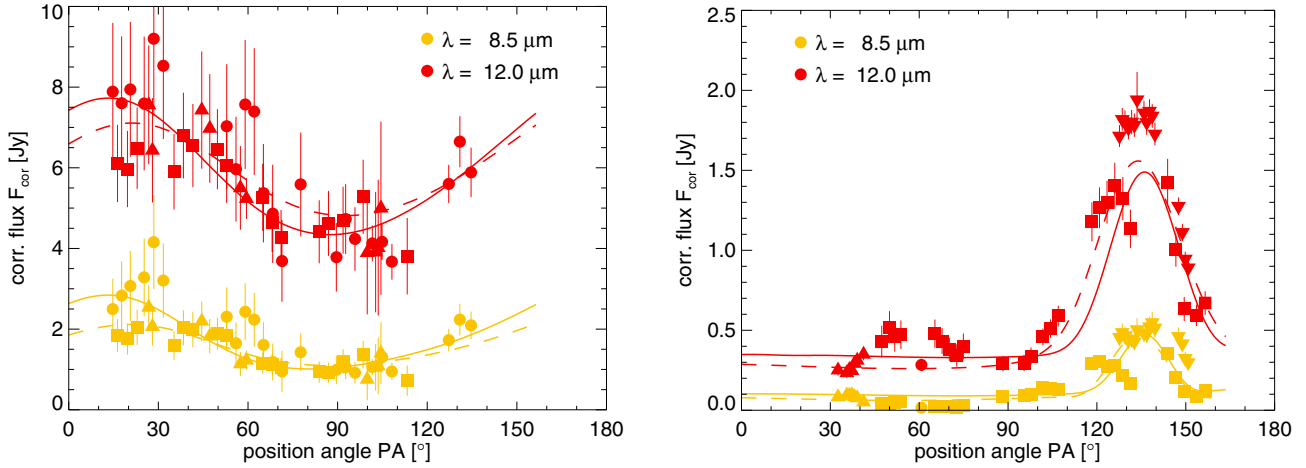


Fig. 6. Correlated fluxes of the Circinus galaxy at 8.5 and 12.0 μm as a function of the position angle for the baselines E0-G0 (with $13 \text{ m} < \text{BL} < 16 \text{ m}$, *left*) and UT2-UT4 (with $76 \text{ m} < \text{BL} < 90 \text{ m}$, *right*). Also plotted are the correlated fluxes of the three-component model discussed in Sect. 4: fit 3 by continuous lines, fit 2 and 1 by dashed lines in the *left* and *right* panels, respectively.

is not present at 8.5 μm . We interpret this behaviour as evidence of further small scale structure. Finally, the 12.0 μm fluxes are always above $\sim 0.3 \text{ Jy}$, indicating that there is still unresolved flux at these wavelengths. The fluxes at 8.5 μm are consistent with zero at $\text{PA} \sim 60^\circ$. Thus the 8.5 μm emission is completely resolved out by the interferometer.

In summary, we conclude from the direct and completely model free analysis of the data that there are two different orientations in the mid-infrared brightness distribution of the Circinus galaxy: on spatial scales of $\sim 150 \text{ mas}$ the emission is moderately elongated along $\text{PA} \sim 90^\circ$, while on smaller spatial scales, the emission is highly elongated along $\text{PA} \sim 45^\circ$.

4. Modelling

To get a better understanding of the overall structure of the emission, we model the data. Motivated by the evidence of (1) an essentially unresolved emission component; (2) a small, highly elongated component; and (3) an extended, only slightly elongated component, we expand the two-component model from Tristram et al. (2007) to three components. In the following, we will refer to these three components as $i = 1$ the “unresolved”, $i = 2$ the “disk-like” and $i = 3$ the “extended” components of the emission. Despite being “unresolved”, component 1 has a non-zero size because its brightness depends on its surface and temperature.

The model is not intended to directly represent any physical structure for the emission. To begin with, it is intended to capture the general morphology and spectral properties of the surface brightness distribution of the source, by fitting the interferometric data and the total flux spectrum in the wavelength range between $\lambda = 8.0$ and $13.0 \mu\text{m}$.

The three components are modelled as black-body emitters with a Gaussian brightness distribution. The Gaussian emitters can be elliptical and each emitter is behind an absorption screen responsible for the silicate absorption. For each component, the elliptical Gaussian is a function of the position on the sky (α, δ) and takes the functional form

$$G_i(\alpha, \delta) = f_i \cdot \exp\left[-4 \ln 2 \cdot \left[\left(\frac{\alpha'_i}{r_i \cdot \Delta_i}\right)^2 + \left(\frac{\delta'_i}{\Delta_i}\right)^2\right]\right], \quad (1)$$

where $\alpha'_i = (\alpha - \alpha_i) \cdot \cos \psi_i + (\delta - \delta_i) \cdot \sin \psi_i$ and $\delta'_i = (\alpha - \alpha_i) \cdot \sin \psi_i - (\delta - \delta_i) \cdot \cos \psi_i$ are the positional coordinates of the

Gaussians, which are offset by (α_i, δ_i) from the centre and rotated by the position angle ψ_i . f_i specifies the maximum surface filling and emissivity factor of this component at the position (α_i, δ_i) , Δ_i is the full width half maximum (FWHM) of the Gaussian along its major axis (oriented along ψ_i), and r_i is the ratio of the minor to major FWHM. A maximum surface filling factor of 1 is possible for the sum of all three components. This was not handled entirely correctly in the modelling in Tristram et al. (2007). There, the emission of the two components was simply added one to another, which could effectively result in a total filling factor greater than one. This physical inconsistency, however, did not have any consequences on the overall results. Now we take this additional, physical constraint into account, and use modified Gaussians calculated as

$$\tilde{G}_i(\alpha, \delta) = \left[G_i(\alpha, \delta) - \left(\left(\sum_{j=1}^i G_j(\alpha, \delta) - 1 \right) > 0 \right) \right] > 0. \quad (2)$$

The final flux density of the model at a certain wavelength λ is given by

$$F(\lambda, \alpha, \delta) = \sum_{i=1}^3 \tilde{G}_i(\alpha, \delta) \cdot F_{\text{BB}}(T_i, \lambda) \cdot e^{-\tau_i \cdot \tau(\lambda)}, \quad (3)$$

where F_{BB} is the black-body intensity depending on the temperature T_i , and τ_i is the optical depth of the silicate feature. For the extended component ($i = 3$), the optical depth can linearly change along the major axis, i.e. $\tau_3(\alpha, \delta) = \tau_3 + \xi_3 \cdot d$, where d is the distance from $(\alpha, \delta) = (0, 0)$ projected onto the major axis. This gradient is a first approximation for the overall change of the silicate absorption depth and is motivated by the gradient seen in the mid-infrared spectra by Roche et al. (2006). It will be discussed in more detail in Sect. 5.2.2. The template absorption profile $\tau(\lambda)$ is the same as in Tristram et al. (2007), i.e. it is derived from the extinction curves of Schartmann et al. (2005) and Kemper et al. (2004).

In total, the model has 25 parameters (8 for each component plus ξ_3). However, because the innermost component is assumed to be essentially unresolved, it is not elongated, and thus $\psi_1 = 0$ and $r_1 = 1$. Furthermore, because MIDI only measures differential phases and not the full Fourier phases (see Sect. 2.2), the absolute position on the sky is undetermined. We therefore

define the disk-like component to lie at the origin of our coordinates, that is $(\alpha_2, \delta_2) \equiv (0, 0)$. Furthermore, the offset of the extended component is not well constrained and it does not lead to a significant improvement of the fit (see below). We therefore also assume the extended component to be located at the centre, $(\alpha_3, \delta_3) \equiv (0, 0)$. The coordinates of the unresolved component are therefore to be interpreted as offsets with respect to the other components. We are then left with up to 19 free parameters in the model. To carry out the fit, the brightness distribution of the model is calculated for $8.0 \mu\text{m} < \lambda < 13.0 \mu\text{m}$, then Fourier transformed to obtain the complex correlated fluxes:

$$\mathcal{F}(\lambda, u, v) = \iint d\alpha d\delta F(\lambda, \alpha, \delta) e^{-2\pi i(u\alpha + v\delta)/\lambda}. \quad (4)$$

The moduli of the correlated fluxes, $F_{\text{corr}} = |\mathcal{F}|$, and the wavelength differential phases, ϕ_{diff} , are extracted at the measured uv points and compared to the measurements. All calculations are carried out in IDL using custom programmes and employ the programme MPFIT (Markwardt 2009) for non-linear least squares fitting.

Because the components are self-similar and can become degenerate, we first fit certain parts of the uv plane separately. This approach allows us to understand the source morphology on the different spatial scales (cf. Sect. 3) first, before fitting for the entire brightness distribution. In fit 1, we fit the data from baseline U2-U4 only using the two inner components ($i = 1, 2$); in fit 2, we fit the data with BL < 20 m (essentially baseline E0-G0) using the extended component ($i = 3$). The parameters of the remaining components are kept fixed. Only in fit 3, is all the data fitted by all three components, using the parameters of the previous fits as first guesses. The best fit parameters for all three fits are listed in Table 4.

For fit 1, the extended component is suppressed by setting $f_3 \equiv 0$. It can be omitted entirely because the flux from this component is almost completely resolved out ($V < 2\%$) for BL > 70 m. Therefore, the correlated fluxes on the baseline U2-U4 primarily depend on the inner two components. The two components can reproduce the general trends of the data ($\chi_{\text{red}}^2 = 5.2$, dashed lines in the right panel of Fig. 6). The strong increase in the correlated flux at PA $\sim 130^\circ$ is well reproduced by the strong elongation of component $i = 2$. For this reason, it is called “disk-like”, which will be discussed in more detail in Sect. 5.1.1. Due to the well measured position angle dependence of this peak, the position angle of this elongated component is well determined. On the other hand, second order variations of the correlated flux, such as the second peak at PA $\sim 60^\circ$ (see Sect. 3.2) or changes in the spectral shape, are not reproduced by our simple model. They require a more complex brightness distribution. The differential phases can be at least qualitatively reproduced to some degree by an offset of the unresolved component from the disk-like component.

For fit 2, the two inner components are included in the fit because they contribute significantly to the correlated flux. However, their parameters are held fixed at the (approximate) values of fit 1. Because the AT data changes more smoothly as a function of position in the uv plane and because it has larger uncertainties, both the correlated fluxes as well as the differential phases can be well modelled by the extended component ($\chi_{\text{red}}^2 = 1.1$, dashed lines in the left panel of Fig. 6). In fact, the extended component alone is sufficient to achieve the good fit; the inner two components are not required to model the AT data.

Finally, in fit 3, all free parameters are fitted using the 152 correlated flux spectra and differential phases as well

Table 4. Parameters of the three-component Gaussian fits.

i	parameter	Fit 1	Fit 2	Fit 3
		baseline U2-U4	BL < 20 m	all baselines
1: unresolved	α_1 [mas]	2.9^{+15}_{-18}	(3.0)	$-8.5^{+7.0}_{-2.8}$
	δ_1 [mas]	6.5^{+10}_{-24}	(6.0)	$11.6^{+2.6}_{-4.4}$
	Δ_1 [mas]	$10^{+14}_{-1.2}$	(10)	12 ± 2
	τ_1	$0.80^{+1.0}_{-0.5}$	(0.8)	$1.23^{+0.15}_{-0.24}$
	T_1 [K]	264^{+35}_{-22}	(260)	317 ± 22
	f_1	(1.00)	(1.0)	$0.49^{+0.29}_{-0.17}$
2: disk-like	Δ_2 [mas]	45 ± 11	(45)	57 ± 15
	r_2	$0.17^{+0.20}_{-0.06}$	(0.17)	0.16 ± 0.04
	ψ_2 [$^\circ$]	44 ± 6	(44)	46 ± 3
	τ_2	$1.92^{+0.19}_{-0.43}$	(2.00)	1.88 ± 0.40
	T_2 [K]	288^{+32}_{-11}	(290)	290^{+22}_{-13}
	f_2	(1.00)	(1.00)	$0.55^{+0.24}_{-0.14}$
3: extended	Δ_3 [mas]	–	92^{+10}_{-4}	93^{+6}_{-12}
	r_3	–	0.60 ± 0.12	$0.45^{+0.07}_{-0.05}$
	ψ_3 [$^\circ$]	–	114 ± 3	107 ± 8
	τ_3	–	$2.71^{+0.36}_{-0.08}$	$2.40^{+0.1}_{-0.6}$
	ξ_3 [arcsec $^{-1}$]	–	30^{+3}_{-4}	27 ± 6
	T_3 [K]	–	297^{+145}_{-3}	304^{+62}_{-8}
f_3	(0.0)	$0.33^{+0.08}_{-0.26}$	$0.34^{+0.03}_{-0.22}$	
	χ_{red}^2	5.22	1.06	6.32

Notes. Parameters held fixed at certain values are enclosed in parentheses. The parameters for each of the three components $i = [1, 2, 3]$ are: (α_i, δ_i) – position; Δ_i – FWHM; r_i – axis ratio; ψ_i – position angle; τ_i – silicate optical depth; ξ_i – gradient of the silicate optical depth; T_i – temperature; f_i – surface filling factor. See text for details.

as the averaged total flux spectrum. For this fit, we obtain a relatively high value of the reduced chi-squared, $\chi_{\text{red}}^2 = 6.3$. This means that our simple model is not a “good” fit to the full data set; it only traces the general structure of the emission. Nonetheless the quality of our fit is comparable to the similar fit (also using three components) of the correlated fluxes and differential phases in NGC 1068, where $\chi_{\text{red}}^2(\text{NGC 1068}) = 6.2$ (López-Gonzaga et al. 2014). To determine a possible offset of the extended component like in NGC 1068, we carried out a parameter scan for α_3 and δ_3 . Although we find a best fit for $(\alpha_3, \delta_3) = (-45, 3)$ mas with $\chi_{\text{red}}^2 = 6.0$, we also find very different offsets with similarly good values of χ_{red}^2 . Due to this ambiguity and the only small improvement of the fit, we see no compelling evidence for a particular offset of the extended component and therefore set $(\alpha_3, \delta_3) \equiv (0, 0)$. The correlated fluxes of fit 3 are compared to the data as a function of the position angle in Fig. 6 (continuous curves). The dispersed correlated fluxes and differential phases of this fit for all uv -points are plotted in red in Figs. A.1 and A.2.

The formal fit errors calculated from the covariance matrix are very small and not representative of our fit of a smooth model to a more complex emission distribution. To determine more realistic uncertainties for the fit parameters of all three fits, we use the non-parametric bootstrap with replacement (Efron 1979). We employ a block bootstrap (Hall 1985) due to the correlation of consecutively observed uv points, i.e. we resample the data using small sequences of uv points instead of individual uv points before fitting the resampled data. The errors listed in Table 4 are

directly estimated from the bootstrap distribution of the respective parameter and mark the 68.3% (1σ) confidence intervals.

Our model can fit the data on the shortest baselines very well, which means that it reproduces the low spatial frequencies of the source adequately. On longer baselines, however, the data is not well reproduced by our model. This is predominantly due to small scale variations of the correlated fluxes and differential phases at longer baselines (cf. Fig. 4), which cannot be reproduced by our smooth model. We interpret these variations as signatures for small scale structures that our model obviously cannot replicate.

Finally, a few remarks on degeneracies: several parameters of our model are not independent. The clearest example is the degeneracy between the temperature T_i and the surface filling factor f_i . Because we are fitting a narrow wavelength range ($8\mu\text{m} < \lambda < 13\mu\text{m}$), the temperatures of our dust components are not well constrained. A small change in temperature has a direct influence on the brightness of the source, which can be compensated by changing the surface filling factor. Similar degeneracies are present between the size and the axis ratio of the source, which all change the emitted flux density. Depending on how well these parameters are constrained by the interferometric measurements, these parameters can become degenerate.

5. Discussion

5.1. Morphology

The direct analysis of the data (Sect. 3) and our modelling (Sect. 4) confirm that the mid-infrared emission in the nucleus of the Circinus galaxy comes from at least two distinct components: a highly elongated, compact “disk-like” component and a moderately elongated, extended component. To some degree, the distinction between the two components is suggested by the two different regimes of the correlated fluxes as a function of the projected baseline length (see Sect. 3.1). Primarily, however, the distinction is suggested by the different orientations of the two components: the two components are elongated roughly perpendicular to one another. Two clearly separated emission components have also been found in NGC 1068 and NGC 3783 (Raban et al. 2009; Hönig et al. 2013), and a two-component morphology in the infrared appears to be common to a large number of AGN (Kishimoto et al. 2011b; Burtscher et al. 2013).

We interpret the mid-infrared emission as emission from warm dust in the context of the hydrodynamic models of dusty tori in AGN by Schartmann et al. (2009), Wada et al. (2009) and Wada (2012). These models find a relatively cold, geometrically thin and very turbulent disk in the mid-plane of the torus, surrounded by a filamentary structure. The latter consists of long radial filaments with a hot tenuous medium in between. We associate the central, highly elongated component in the Circinus nucleus with the dense disk in these simulations, and we interpret the extended mid-infrared emission in the context of the filamentary torus structure seen in these models.

A false-colour image of our best fitting model (fit 3) is shown in Fig. 7, with the model images at $13.0\mu\text{m}$, $10.5\mu\text{m}$ and $8.0\mu\text{m}$ mapped to the red, green and blue channels of the image, respectively.

When interpreting our observations, we have to take into account that the emission is dominated by the warmest dust at a certain location, which normally comes from the dust clouds directly illuminated by the central UV source. There are probably also considerable amounts of cooler dust. However, the cooler

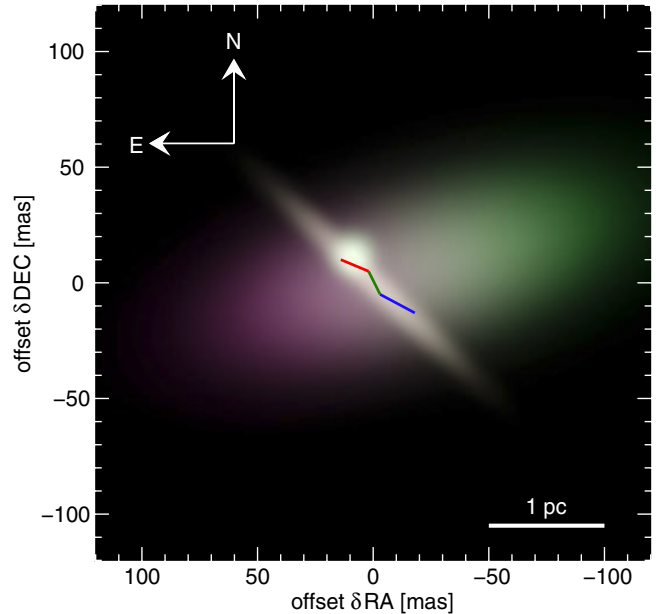


Fig. 7. False-colour image of the three-component model for the mid-infrared emission of the nucleus of the Circinus galaxy (fit 3). The colours red, green and blue correspond to the model at $13.0\mu\text{m}$, $10.5\mu\text{m}$ and $8.0\mu\text{m}$, respectively. The colour scaling is logarithmic in order to show both bright and faint features. Clearly the colour gradient of the extended component due to the increase in the silicate depth towards the south-east is visible. This colour gradient leads to a chromatic photocentre shift towards the north-west. Despite the lower surface brightness, 80% of the emission comes from the extended component. Also plotted is the trace of the water maser disk: the blue and red parts trace the approaching and receding sides of the maser disk respectively. Note that the relative offset of the mid-infrared emission with respect to the maser disk is not known (see text for details).

material only contributes insignificantly to the infrared emission (see also Sect. 5.3).

5.1.1. The disk-like component

The disk-like component is highly elongated and has a major axis FWHM of $\Delta_2 \sim 1.1$ pc. Due to the strong position angle dependency of the correlated fluxes for the longest baselines, the position angle of the major axis is very well constrained: $\psi_2 = 46 \pm 3^\circ$. The strong elongation of this component with an axis ratio of more than 6 : 1 at first suggests an interpretation as a highly inclined disk, as in Tristram et al. (2007). This interpretation is supported by the close agreement in orientation and size of this component with the warped maser disk from Greenhill et al. (2003). The masers were modelled by a thin disk extending from $r_{\text{in}} \sim 0.1$ pc to $r_{\text{out}} \sim 0.4$ pc. The maser disk is warped with the position angle changing from $29^\circ \pm 3^\circ$ at r_{in} to $56^\circ \pm 6^\circ$ at r_{out} . With a position angle of $\psi_2 \sim 46^\circ$, our disk-like component now matches this orientation much better than previously. The larger size of the mid-infrared disk as compared to the maser disk could be evidence of the disk extending out to larger radii than is probed by the maser emission. We emphasise that the agreement is only in orientation and size, not in the absolute position. With MIDI alone, no absolute astrometry is possible because the absolute phase signal is destroyed by the atmosphere (see Sect. 2.2). By consequence, the relative position between the maser disk and our disk-like component cannot be

determined. In Fig. 7, the disk-like component and the maser disk are plotted centred to allow a good comparison, but the two structures might well be offset with respect to each other.

Due to the strong elongation of the disk-like component, the associated disk would have to be close to edge-on and cannot be very thick. If we assume that the emission comes directly from an infinitesimally thin and flat disk, we can use the observed axis ratio to constrain its inclination: $i > 75^\circ$. Or, if seen edge-on ($i = 90^\circ$), as suggested by the maser emission, we can derive a rough estimate for the maximum thickness of the disk: $r_2 \cdot \Delta_2 < 0.2$ pc.

An interpretation as emission directly from the disk is, however, problematic. Due to the high densities required for maser emission ($n(\text{H}_2) \gtrsim 10^8 \text{ cm}^{-3}$, Kylafis & Norman 1991), we expect the disk to be optically thick and to thus appear in absorption rather than in emission when seen close to edge-on. This is corroborated by the dense disks in the hydrodynamical torus models, which appear as dark lanes in the mid-infrared (see Fig. 8 in Schartmann et al. 2009 for an example). The effect is further enhanced by the anisotropic radiation characteristic of the accretion disk, which emits less energy in the direction of the disk plane. A dense disk, by consequence, appears dark. Our disk-like component, on the contrary, appears in emission.

Instead of the disk itself, we could be seeing the directly illuminated inner rim of a highly inclined disk, similar to what is seen for circumstellar disks (e.g. in KK Ophiuchi, Kreplin et al. 2013). However, the inner rim of the disk, where the dust sublimates, is expected to lie at $r_{\text{sub}} = r_{\text{in}} \sim 0.03$ pc for the Circinus galaxy. This is much smaller than the parsec-sized elongation we observe. In addition, the inner rim is expected to consist of hot dust close to the dust sublimation temperature, which is in disagreement with the warm dust at $T \sim 300$ K suggested by our observations. Only if the inner region of the disk were completely dust free and the inner rim were located at a much larger distance ($r_{\text{sub}} \ll r_{\text{in}} \sim 1$ pc), would the size and temperature of the emission be in agreement with our interferometric observations (see also discussion in Sect. 5.4).

Therefore, two alternative explanations seem more likely: First, the emission could come from directly illuminated dusty material slightly above or below the dense disk, such as filaments of dense material swept up from the disk by turbulence. Or, the warp of the disk allows us to see a part of the disk that is directly illuminated by the central source. From the maser observations, Greenhill et al. (2003) deduce that the western side of the warped disk is oriented such that we can see its surface, which is directly illuminated by the accretion disk (see their Fig. 8). Depending on the exact geometry of the warp and the illumination characteristics of the accretion disk, this could lead to the observed highly elongated mid-infrared emission. More sophisticated radiative transfer calculations will have to be carried out to constrain the possible geometries.

5.1.2. Unresolved component

The additional unresolved emission component is required to explain the measurable correlated fluxes when the disk-like component is otherwise fully resolved out. If, in fit 3, this unresolved component is located north-east of the disk-like component, the fit quality is improved. This is mainly because of a better agreement between the differential phases of the model and the observations, especially for the strong phase signal at $(u, v) \approx (-35, 35)$ m (dark blue points at the beginning of the U3-U4 baseline in Fig. 9). We interpret this as a sign that we are tracing smaller scale structure, e.g. an enhanced part of the

disk-like component, possibly a region with less obscuration leading to the comparatively low silicate optical depth of this emission component. For the following discussion we will therefore consider the unresolved emission as a part of the disk-like emission.

5.1.3. Polar elongated dust

The extended emission component is responsible for $\sim 80\%$ of the emission in the N -band, independent of the wavelength. This can already be seen in Fig. 5, where the visibility quickly drops to values of $\lesssim 20\%$ with increasing baseline length. Similarly high contributions to the total emission from extended dust have been found for NGC 1068 and NGC 3783 (Raban et al. 2009; Höning et al. 2013). There is, however, one significant difference: in these galaxies, the contribution of the extended component depends strongly on the wavelength (e.g. from 55% to 90% between $\lambda = 8.0$ and $13.0 \mu\text{m}$ for NGC 3783). This is not the case in the nucleus of the Circinus galaxy due to the lack of any significant temperature difference between the components (see discussion in Sect. 5.4).

The extended emission is significantly elongated along PA $\sim 107^\circ$, which is roughly (but not exactly) perpendicular to the disk-like component (PA $\sim 46^\circ$) and, thus, in polar direction. In fact, there is mounting evidence that this is a common characteristic of Seyfert galaxies: also in NGC 1068, NGC 424 and NGC 3783 the majority of the emission is extended in polar direction (Poncellet et al. 2007; Raban et al. 2008; Höning et al. 2012, 2013). This obviously raises the question: Where is the dust responsible for this emission located?

The polar dust emission could originate from dust *within* the ionisation cone. Dust clouds inside the ionisation cone or, more generally, the Narrow Line Region may contribute significantly to the mid-infrared emission of AGN (e.g. Radomski et al. 2003; Poncellet et al. 2007; Schweitzer et al. 2008). A contribution of 80% in our case nevertheless appears very high for the following reason. The Circinus galaxy has a sharply delimited ionisation cone, and the central engine is fully obscured along other lines of sight. While the projected half opening angle of the visible ionisation cone onto the plane of the sky is $\vartheta_{\text{proj}} \sim 45^\circ$ (Wilson et al. 2000), the physical half opening angle has been estimated to be $\vartheta_{\text{cone}} \sim 41^\circ$ from modelling of the narrow line kinematics (Fischer et al. 2013). This means that more than 70% of the sky are covered by the equatorial obscurer. Furthermore, the dusty material in the ionisation cone must have a low covering factor, typically $< 30\%$. Therefore, the total covering fraction of the dust in the ionisation cone is most likely $< 10\%$, which is consistent with the estimate by e.g. Mor et al. (2009). It is then difficult to explain why this material is responsible for 80% of the mid-infrared emission, while all the other dust intercepting most of the energy from the central engine radiates much less. Furthermore, the dust emission in the ionisation cone is expected to be optically thin and to show the silicate feature in emission. While this may be the case in NGC 424 (Höning et al. 2012), this is certainly not the case for the Circinus galaxy: the extended emission has, on average, the highest silicate optical depth.

Deep single-dish images of the Circinus nucleus (Packham et al. 2005; Reunanen et al. 2010) already show a faint halo surrounding the nuclear point source. This halo is extended ~ 2 arcsec along PA $\sim 100^\circ$ and 280° . It is interpreted as emission from dense dusty material which enters the ionisation cone preferentially from one direction due to a nuclear gaseous bar and is entrained outward in an outflow possibly driven by radiation pressure (Maiolino et al. 2000; Packham et al. 2005). Our

extended emission component naturally appears as a continuation of this outer halo towards the nucleus. We therefore interpret the extended component as enhanced emission from the southern edge of the ionisation cone, that is from the inner funnel of the torus. The emission from the funnel most likely has smaller scale structure, such as bright regions along the cone edge or along filaments. We consider such smaller scale structures to be responsible for the irregular behaviour of the visibilities and differential phases on longer baselines (cf. Sect. 5.2.3).

In addition to an enhanced supply of material to one side of the ionisation cone, a preferential illumination of the cone edge along PA $\sim -90^\circ$ (and the counter cone along PA $\sim 90^\circ$) may be responsible for the enhanced emission in this direction: the best estimate for the orientation of the accretion disk comes from the innermost disk masers (see Sect. 5.1.1), suggesting a disk axis along -60° . This value also agrees well with the position angle of the radio lobes, PA $\sim 115^\circ$ and $295^\circ = -65^\circ$ (Elmouttie et al. 1998), which are most probably launched in the innermost region of the accretion disk. The flux from a thin, optically thick accretion disk depends on the polar angle ϑ as $F \propto \cos \vartheta (1 + 2 \cos \vartheta)$, i.e. it emits anisotropically with the strongest emission in direction of the disk axis (Netzer 1987). This implies that the radiation towards the edges of the ionisation cone at PA $\sim -90^\circ$ and $+90^\circ$ ($\vartheta \sim 30^\circ$) are more illuminated than the opposite cone edges at PA $\sim 0^\circ$ and 180° ($\vartheta \sim 60^\circ$) by a factor of about two. The unobscured, western cone edge along at PA $\sim -90^\circ$ thus appears brighter.

5.2. Differential phases

5.2.1. Characteristics of the differential phase signal

In our MIDI data, we find relatively strong differential phases with amplitudes (peak-to-valley) of up to $\sim 80^\circ$. The phase signal may be caused either by atmospheric phase residuals (mainly chromatic dispersion due to water vapour) or it may be intrinsic to the source. We are convinced that the signal is intrinsic to the source for the following reasons: (1) in several cases (especially for the measurements using the UTs), the phase measurements have a high signal to noise ratio, $S/N > 5$; (2) the differential phases agree or are very similar when measured twice at different epochs (cf. Sect. 2.3). This is further corroborated by a flip of the differential phase for an interchange of the telescopes. Two examples of such a flip are shown in Fig. 2 (comparisons C4 and C6: bottom row, first and last columns); (3) we see no significant differential phase signal in any other AGN (Burtscher et al. 2013, see their Fig. 63). An exception is NGC 1068, which shows strong differential phases similar to those of the Circinus galaxy (López-Gonzaga et al. 2014). It is unlikely that strong phase residuals remain after calibration only for the two brightest AGN observed with MIDI. It is more likely that we are able to detect their intrinsic phase signal more easily due to their brightness. We thus conclude that the observed differential phase signal is dominated by the intrinsic structure of the brightness distribution.

Differential phases appear if there is an asymmetry in the brightness distribution. This asymmetry does not necessarily have to be chromatic: due to the different spatial frequencies probed by different wavelengths, a phase signal is also introduced for non-chromatic, yet spatially asymmetric sources⁵. We

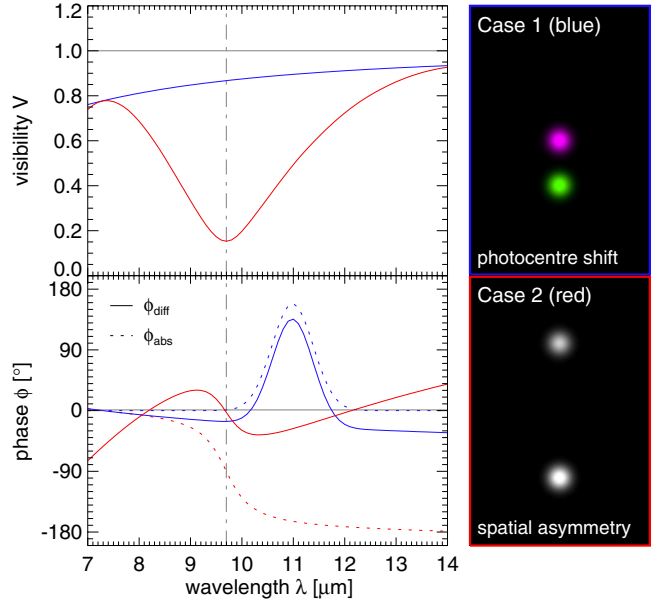


Fig. 8. Examples for the two ways to produce a smooth differential phase signal: (1) a chromatic photocentre shift (blue) and (2) a purely spatial asymmetry of the brightness distribution (red). In case 1, the source is shifted to the bottom between $\lambda \sim 10 \mu\text{m}$ and $12 \mu\text{m}$; in case 2, the “binary” has a brightness ratio of 0.7 : 1.0. The resulting visibilities and phases are shown in the *left panels*, with the absolute Fourier phases ϕ_{abs} and the differential phases ϕ_{diff} (as would be measured with MIDI) plotted by dotted and continuous lines, respectively. In the *right panels*, the two brightness distributions are shown as false-colour images, with the brightness distribution at $13.0 \mu\text{m}$, $11.0 \mu\text{m}$ and $8.0 \mu\text{m}$ mapped to the red, green and blue channels, respectively.

thus distinguish two ways to produce a differential phase signal in our MIDI data (Fig. 8, see also Deroo et al. 2007):

1. A chromatic photocentre shift of a brightness distribution that is otherwise point-symmetric at each wavelength (plotted blue in Fig. 8). The photocentre shift has to be nonlinear in wavenumber to produce a differential phase signal measurable with MIDI. An example of this is a point-symmetric brightness distribution that is shifted in one direction in an emission line. In this first case, the correlated fluxes (and visibilities) of the source remain *unchanged* with respect to a source with no photocentre shift.
2. A brightness distribution that is asymmetric at each wavelength but otherwise has the same spectrum everywhere. In this case, the differential phases are caused by phase gradients (“jumps”) of the complex visibilities as they are probed at different spatial frequencies for different wavelengths. An example is a binary with unequal brightness but identical spectrum (plotted red in Fig. 8). For such a binary, the differential phases appear as a smoothed step. The amplitude and the smoothing of the step depends on the brightness ratio of the two components⁶. For this second case, the phase jump occurs at a *minimum* of the visibilities (cf. top left panel in Fig. 8). This is in contrast to case one, where the visibilities remain unchanged.

the point where $V = 0$. This has been measured, e.g. for the star Vega (Schmitt et al. 2006). Because we do not see such sharp phase jumps in the data of the Circinus galaxy, we do not further consider these special cases here.

⁶ In the case of an equal binary, the jump is exactly 180° and sharp at the spatial frequency where the complex visibility changes sign, similar to the case of a ring or uniform disk.

⁵ In fact, even symmetric, non-chromatic brightness distributions can have a phase signal, as the examples of a ring or a uniform disk show. In these cases, however, there is a sharp phase jump by exactly 180° at

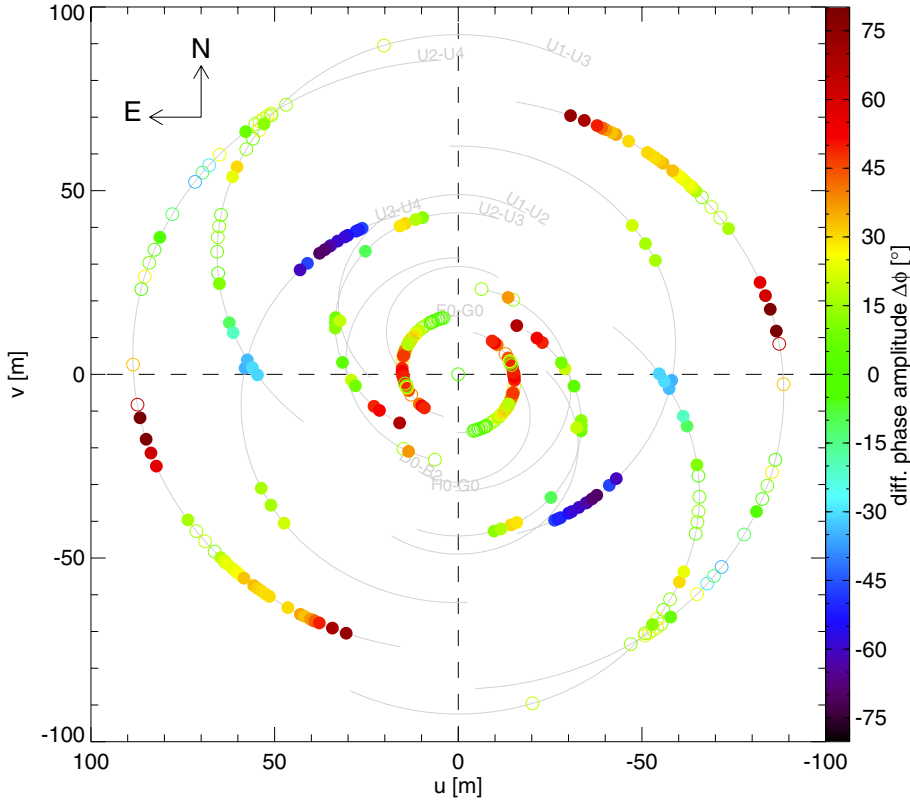


Fig. 9. Amplitude of the differential phases in the uv plane: each uv point is colour-coded with the value of $\Delta\phi$, the difference of the differential phase at $10\ \mu\text{m}$ to those at the edges of the N -band ($\lambda = 8.2\ \mu\text{m}$ & $13.0\ \mu\text{m}$). Filled dots denote a phase signal with $>3\sigma$ significance averaged over the N -band, empty circles a phase signal with $<3\sigma$ significance, i.e. a differential phase consistent with 0.

Typically, in interferometry, a mixture of both cases occurs and it is hard to separate the two effects. For example in a binary, the two companions usually have different spectral types. Short of being able to fully reconstruct the true wavelength-dependent brightness distribution of the nuclear dust in the Circinus galaxy, we will use the discussed properties of the differential phases to derive some information on the asymmetries of the brightness distribution.

In general, the differential phases of the Circinus galaxy change smoothly over the entire N -band, without any sharp phase jumps. Figure 9 shows the amplitude of the differential phase signal, $\Delta\phi = \phi_{\text{diff}}(10.0\ \mu\text{m}) - \frac{1}{2}(\phi_{\text{diff}}(8.2\ \mu\text{m}) + \phi_{\text{diff}}(13.0\ \mu\text{m}))$, in the uv plane. Differential phases with more than 3σ significance (averaged over $8.2\ \mu\text{m} < \lambda < 13.0\ \mu\text{m}$) are plotted by filled dots. Phases which are consistent with $\Delta\phi = 0$ are plotted by open circles. A negative value means the phase has a concave (U-shaped) dependency, while positive values mean the phase has a convex shape (i.e. \cap -shaped). To make the plot easier to read, $\Delta\phi$ was corrected for an interchange of the telescopes.

Clearly there are distinct areas in the uv plane with strong differential phases. Furthermore, we find equally strong differential phases on large spatial scales (short baselines) as on small spatial scales (long baselines). This directly implies that not only small scale structure (“clumps”) can be made responsible for the phase signal. These would only produce a phase signal on the longest baselines.

5.2.2. The phase signal of the large scale structure

On the shortest baseline (E0-G0), we measure a phase signal of up to $\Delta\phi = 70^\circ$, with a more or less smooth dependency of $\Delta\phi$ on the position angle. For $\text{PA} \sim 15^\circ$ to 30° the differential phase is consistent with zero, then increases to reach its maximum

between $\text{PA} \sim 80^\circ$ and 140° . Furthermore we find that the phase signal is somewhat V-shaped, reminiscent of the shape of the silicate absorption feature. This and the smooth dependency with position angle strongly suggest that the phases are dominated by large scale variations of the silicate absorption strength, consistent with case 1 discussed above. Indeed, the differential phases on the shortest baselines can be very well explained by a linear gradient of the optical depth of the silicate feature over the source. In our modelling, we applied a linear gradient in the optical depth to the extended component of our three-component model (see Sect. 4): $\tau_3(\alpha, \delta) = \tau_3 + \xi_3 \cdot (\delta \cdot \cos \psi_3 + \alpha \cdot \sin \psi_3)$. Consistent with the position angle dependence of the phase signal, the gradient is oriented in direction of the major axis of this component. A gradient in the optical depth effectively leads to a shift of the emission in the direction of lower absorption (see also Fig. 7). The shift is towards the north-west, and it is non-linear in wavelength due to the specific wavelength dependency of the silicate optical depth. In fact, an enhancement of the emission towards the north-west was already suggested in Tristram et al. (2007).

From our model fit, we find a gradient of the optical depth of $\xi_3 \sim 27\ \text{arcsec}^{-1}$. The positive value means that the silicate absorption depth increases towards the south-east, i.e. this side of the nucleus is more heavily obscured. This is consistent with observations at larger scales, where the south-eastern sides of the inclined galactic disk (Freeman et al. 1977) and a circumnuclear molecular ring (Curran et al. 1998, 1999) are located closer to us. Furthermore, the ionisation cone is one-sided towards the north-west (e.g. Marconi et al. 1994; Wilson et al. 2000), and colour maps (e.g. Prieto et al. 2004) show redder colours towards the south-east – all implying stronger obscuration towards the south-east. The highly inclined nuclear maser disk is the only structure with a size directly comparable to our dust distribution. Our results would be most consistent if the south-eastern side of the warped disk is located closer to us, similar to the galactic scale

structures and as somewhat implied by Greenhill et al. (2003). It appears that the Circinus galaxy is more heavily obscured towards the south-east all the way down to the very nucleus. The disk-like obscurers on different spatial scales (the galactic disk, the circumnuclear ring and the nuclear disk) all have the north-western part of their axes slightly directed towards us.

The rather large gradient in the silicate absorption depth is necessary to obtain a significant colour change on scales of less than 100 mas. Using long-slit spectroscopy in the mid-infrared, Roche et al. (2006) mapped the strength of the silicate feature along PA = 10° and PA = 100°. They found a general trend of the optical depth along PA = 100°, increasing from $\tau_{9.7\ \mu\text{m}} \sim 1.0$ at 1.3 arcsec west of the nucleus to $\tau_{9.7\ \mu\text{m}} \sim 2.6$ at 1.3 arcsec east of the nucleus. A similar trend is not found along PA = 10°. These measurements further support that the south-eastern side of the nucleus is more obscured. The observed large scale trend corresponds to a gradient of $\xi_{\text{Roche}} \sim 0.6\ \text{arcsec}^{-1}$. This is more than one order of magnitude less than our result. Such a low gradient would not produce a significant phase signal in the interferometric measurements by far. Therefore, our gradient cannot be directly connected to the larger scale obscuration on scales of tens of parsecs. We instead interpret our strong colour gradient as evidence of more dense dusty material on scales of less than an arcsecond (i.e. less than 20 pc). This is consistent with evidence for much of the obscuration in the nucleus taking place on parsec scales (Prieto et al. 2004).

5.2.3. The phase signal for high spatial frequencies

For higher spatial frequencies (smaller scales, measured with longer baselines) the interpretation of the phase signal is more difficult. The amplitude and the shape of the differential phases change significantly between different locations in the uv plane. While some areas have a strong phase signal of up to $\Delta\phi = 90^\circ$, the measurements are consistent with no significant phase signal in other areas. In contrast to the phases on the shortest baselines, there is no preferential direction, and we find no general correlation (or anti-correlation) of $\Delta\phi$ with F_{cor} . There seem to be “patches” of stronger phases in different areas of the uv plane. In particular, we see no general trend for the phase signal to be strongest at minima in the correlated fluxes. This argues against the phase signal being caused by purely achromatic asymmetries (case 2, see Sect. 5.2.1). We therefore suspect colour gradients and especially changes in the optical depth on intermediate scales to be responsible for these phases.

An exception are the uv points at $(u, v) \approx (33, 14)$ m. These correspond to the comparison C5 (see Sect. 2.3). The correlated fluxes and differential phases for this location in the uv plane are shown in the middle column of Fig. 2. Clearly, the correlated flux (and the visibility) has a dip at $\lambda \sim 12.4\ \mu\text{m}$ which strongly deviates from the normal spectral shape of the Circinus galaxy. The dip is at the same wavelength as a strong gradient and zero-crossing of the differential phase, suggestive of case 2 discussed in Sect. 5.2.1. This means a discrete asymmetry is probed by these measurements (and only by these measurements!). A closer inspection of the data reveals that the wavelength at which the minimum occurs varies slightly from $\lambda = 12.3\ \mu\text{m}$ to $\lambda = 12.5\ \mu\text{m}$ for the individual measurements. This is roughly followed by corresponding changes of the zero-crossing of the differential phases, as we would expect for a phase jump at a visibility minimum. Assuming an unequal binary, we can directly calculate the projected separation d_{proj} of the two components: as can be derived easily, the separation is given by

$d_{\text{proj}} = \lambda_0/\text{BL}_0 \cdot (2n+1)/2$, where λ_0 and BL_0 are the wavelength and projected baseline length at which the minimum in the visibilities and the phase jump occur, and $n \in \mathbb{N} = [0, 1, 2, 3, \dots]$. In our case, we obtain $d_{\text{proj}} = (2n+1) \cdot 35.5\ \text{mas}$. Note that only $n = 0$ appears likely, because separations of more than 100 mas are unlikely considering the overall size of the emission. Also, for higher values of n , we would quickly start observing more than one step in the phases within $8.0\ \mu\text{m} < \lambda < 13.0\ \mu\text{m}$. In any case, the separation is intermediate between the sizes of the inner disk-like component and the extended dust component. It is certainly too large to be attributed to individual clumps of the torus. It instead indicates intermediate scale asymmetries in the brightness distribution, as could be caused by warps in the inner disk-like component or enhanced emission regions along the inner edge of the dust distribution (cf. Sect. 5.1.3).

We conclude that the strong differential phases observed on longer baselines provide evidence of intermediate scale asymmetries in the dust emission, both chromatic and achromatic, caused by the specific illumination and geometry of the dust distribution. Interferometric observations enabling image reconstruction on the one hand and more sophisticated modelling on the other hand will be required to reveal the details of the underlying brightness distribution.

5.3. Spectral energy distribution

To be meaningful, our model has to not only reproduce the interferometric data in the N -band, but also be consistent with the entire SED of the Circinus galaxy. The SED of the Circinus galaxy from Prieto et al. (2010) is shown in Fig. 10. With an angular resolution of $<1.5\ \text{arcsec}$, these measurements represent the true nuclear SED. We add to this SED a new measurement of the continuum emission at $\lambda = 9.3 \times 10^{-4}\ \text{m}$ (321 GHz) obtained by Hagiwara et al. (2013) with ALMA: $F_{\text{ALMA}} = 55\ \text{mJy}$. Low resolution measurements with IRAS (Moshir et al. 1990) are plotted as blue crosses for reference. The error bars correspond to an assumed uncertainty of 0.1 dex for all photometric data points (e.g. due to variability). A MIDI correlated flux spectrum (#41, BL = 87 m, selected for its low correlated flux and good S/N) is plotted in cyan, and the averaged total flux spectrum from MIDI is plotted in blue. The SED of our model is shown in red. For comparison, we also reproduce the high spatial resolution spectrum of the inner 0.81 arcsec from Roche et al. (2006) in grey.

Not surprisingly, the SED of our model closely resembles the Planck curve for a black body of $T \sim 300\ \text{K}$, with some modifications due to absorption, most notably the silicate features at $\lambda = 9.7\ \mu\text{m}$ and $20\ \mu\text{m}$. Although we only fitted our model to the data obtained with MIDI, it is consistent with the entire high resolution SED: it represents the flux in the mid-infrared well while producing less or equal flux at other wavelength ranges.

At the long wavelength end of the N -band (see inset of Fig. 10) our model under-predicts the total flux spectrum for $\lambda \gtrsim 12\ \mu\text{m}$. We interpret this as evidence of additional, cooler dust, which is responsible for this emission and which is not fully captured by our model. On the other hand, the measurement with ALMA sets a strong constraint on the emission from cooler dust in the innermost 1.3 arcsec (26 pc) of the Circinus galaxy. While the SED of our model is consistent with the ALMA measurement, it rules out any major contribution to the SED from additional dust in the nucleus with $T < 200\ \text{K}$. This is consistent with the results of radiative transfer calculations of dusty tori, which

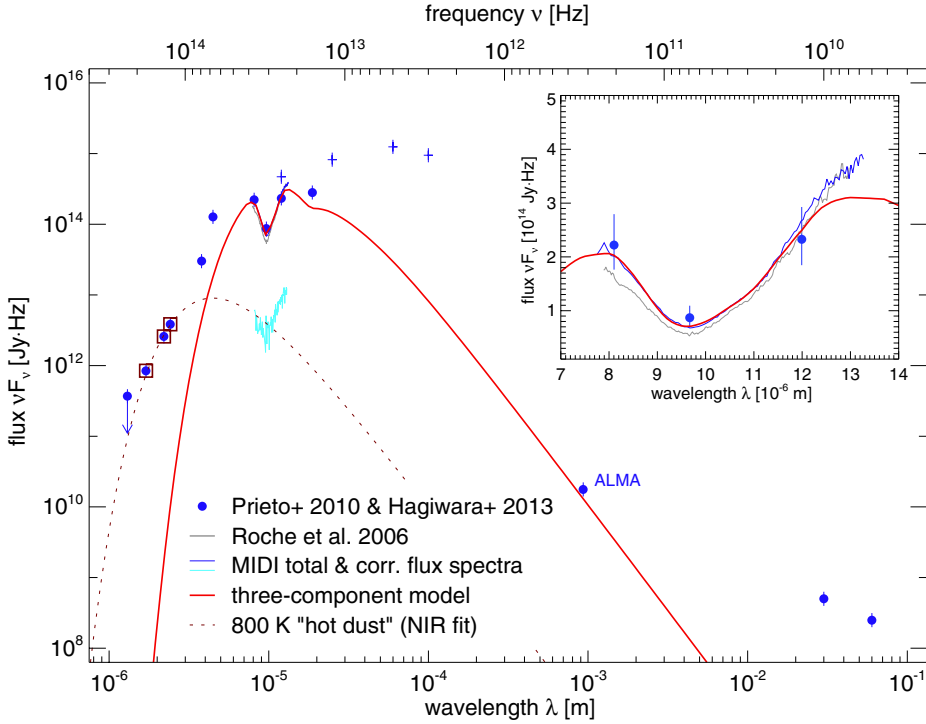


Fig. 10. Nuclear SED of the Circinus galaxy. Blue dots are high resolution photometry compiled by Prieto et al. (2010) plus an additional measurement with ALMA at $\lambda = 9.3 \times 10^{-4}$ m (321 GHz) by Hagiwara et al. (2013). The measurement in the *J*-band, which is only an upper limit, is marked with an arrow. Also shown are low resolution IRAS photometry (blue crosses), a MIDI correlated flux spectrum (cyan line), the averaged MIDI total flux spectrum (blue line) and the high resolution spectrum from Roche et al. (2006, grey line). The SED of our best fitting model is plotted in red. A possible compact hot dust component, fitted to the SED data marked by the dark red boxes, is shown by the dotted, dark red line. A zoom on the *N*-band region with linear scaling of the axes is shown as an *inset*. See text for further details.

in general show a steep decrease in the torus SED towards longer wavelengths.

Towards shorter wavelengths, the model SED rapidly decreases following the (absorbed) Wien tail of the black-body emission. The observed SED in the near-infrared is much higher. The observed fluxes in the *J*, *H* and *K*-bands are compatible with an additional compact component of hot dust ($T \sim 800$ K, dotted curve in Fig. 10). Such a component would not contribute significantly to the emission in the mid-infrared. It would still be (marginally) consistent with the lowest correlated fluxes measured with MIDI, which can be considered as upper limits for any contribution by a compact hot emission component (e.g. the cyan curve in Fig. 10). However, our interferometric measurements rule out a compact emitter that produces sufficient flux to explain the photometric measurements in the *L* and *M*-band. We tested this by fixing the temperature of the unresolved component to $T_1 = 600$ K and adjusting f_1 so that the near-infrared part of the SED is reasonably well reproduced. We then obtain much higher correlated fluxes than observed at the short wavelength end, unless $\Delta_1 \gtrsim 15$ mas. This means that most of the emission at these wavelengths must be extended by at least 0.3 pc and less than 3.8 pc (190 mas, unresolved by single dish observations). This is discussed further in Sect. 5.4.

In conclusion, we find that our model is consistent with the overall SED of the Circinus galaxy. We further conclude that the nuclear SED is dominated by emission from dust close to $T \sim 300$ K and that the contribution from dust at much hotter ($T > 800$ K) or cooler ($T < 200$ K) temperatures is very low on parsec scales.

5.4. Lack of a compact hot dust component

In Tristram et al. (2007), no significant temperature gradient was found in the dust distribution of the Circinus galaxy. One of the main goals of the new observations was to search for hotter dust using longer baselines, or generally for an increase in the dust temperature towards the centre, similar to what is observed in

NGC 1068 (Jaffe et al. 2004; Raban et al. 2008; López-Gonzaga et al. 2014). NGC 1068 is similarly well resolved (both in terms of visibility and scales of the supposed sublimation radius) as the Circinus galaxy. In NGC 1068, the correlated fluxes are on average bluer than the total flux ($F_{\text{cor}}(13 \mu\text{m})/F_{\text{cor}}(8 \mu\text{m}) < F_{\text{tot}}(13 \mu\text{m})/F_{\text{tot}}(8 \mu\text{m})$). This clearly indicates an increase in the dust temperature towards the centre. In the Circinus galaxy, however, the emission at the short wavelength end of the *N*-band is almost completely resolved out even on the longest baselines, and we see no significant difference between the temperatures of our model components (for all three components, $T \sim 300$ K). The new measurements thus confirm the earlier results: we find no evidence of a temperature increase towards the centre. This is unexpected, because the resolution limit of our interferometric observations, ~ 0.1 pc, corresponds to a few times the sublimation radius ($r_{\text{sub}} \sim 0.03$ pc). We should start seeing hotter dust on these scales.

There are two possible explanations for the lack of hot dust at the centre: either we (still) cannot see it, or it is truly absent. In the first case, the hot dust component could be so highly obscured on scales of a few r_{sub} that we simply do not see it. However, this is somewhat in contradiction with the decrease in the silicate absorption depth towards the centre unless the innermost dust contains less silicates. Full radiative transfer calculations will have to be carried out to verify if a hot dust component can be fully obscured while reproducing the other characteristics of the Circinus nucleus. In the second, more speculative case, there might simply be no hot dust at the inner rim of the torus at all. In Sect. 2.3.2, we discussed a possible variability in the Circinus galaxy. It is therefore conceivable that the active nucleus was previously in a more active state or even that an explosive event occurred some time ago (Bland-Hawthorn et al. 1997). The increased activity would lead to an increased sublimation radius. If the inner rim were to contract only slowly after the activity decreased, the innermost dust would be at much cooler temperatures for some time. Such a large and relatively cool inner rim would not only explain the lack of hot dust but also

the highly elongated disk-like component (cf. Sect. 5.1.1). On the other hand, this would require very long timescales for dust formation, preventing the inner rim from quickly moving back inwards. The amplitude of variability would have to be three to four orders of magnitude to result in a significantly cooler inner rim. Moreover, the near-infrared excess of the SED with respect to our model indicates that dust at $T > 500$ K must exist (see Sect. 5.3).

The explanations are not very satisfactory. Furthermore, the problem is not the lack of a hot dust component alone, but rather the absence of any evidence of an increase in the dust temperature towards the centre. The interferometric measurements roughly probe spatial scales from 20 to 200 mas (0.4 to 4.0 pc). If we include our single dish measurements or the spectra observed by Roche et al. (2006), the spatial scales explored are up to 500 mas (~ 10 pc) or 2 arcsec (~ 40 pc), respectively. The temperature of directly illuminated dust⁷ depends on the distance as $T \propto (L/r^2)^{1/5.6} \propto r^{-1/2.8}$ (Barvainis 1987). Consequently, we would expect a temperature difference by a factor of $(25/170)^{-1/2.8} \approx 2$ in the range of the interferometric measurements, or a temperature change by a factor of more than 3 when including the single dish data. This is clearly not observed. This lack of a temperature gradient poses a challenge for the picture of a centrally heated dust distribution in the nucleus of the Circinus galaxy.

5.5. What is the “dusty torus”, and where is it?

A central question is, of course, which of the observed components can be associated with the dusty torus in unified schemes of AGN? Here we consider the “torus” defined by its role in classical unification schemes: it obscures the central engine for certain (edge-on) viewing angles while at the same time collimating the ionising radiation and outflows. Additionally, the dust in the inner funnel of the torus scatters emission from the central engine towards an observer. The Circinus galaxy certainly shows all these characteristics of a dusty torus (see Sect. 1).

One explanation for the obscuration and collimation could be a constant scale height of the inner disk, or even a puffed-up inner rim within a few r_{sub} , similar to what has been suggested for disks around young stellar objects (Natta et al. 2001; Dullemond et al. 2001). The latter scenario has recently also been proposed for AGN (Hönig et al. 2012). However, if the obscuration and collimation already take place within a few r_{sub} (i.e. within ~ 0.1 pc for the Circinus galaxy), then the material in the disk at larger radii should be shadowed and significantly colder than 300 K. This contradicts the parsec-sized, equatorially extended emission of our disk-like component as well as the requirements for the pumping of the disk masers, which require a direct line of sight to the central engine (Greenhill et al. 2003; Lo 2005). Also, such a geometry is hard to reconcile with the outflow (120° opening angle) traced by water masers on sub-parsec scales, which implies that the material is still not fully collimated on these spatial scales.

We therefore argue that most of the collimation (and with it obscuration) most likely take place on scales of ~ 1 pc, surrounding the disk. This is consistent with the disk masers and the inner wide angle outflow not extending beyond this scale and the large scale structures having been collimated within a few parsec. In this picture, a significant part of the polar elongated emission originates from the inner funnel of the obscuring

material, which is equivalent to the outer edge of the ionisation cone (see Sect. 5.1.3). Most of the obscuration and collimation is not due to the disk, but due to the material located above or below it. We therefore consider that it is this material which is commonly associated with the “obscuring torus” in AGN.

6. Summary and conclusions

We have obtained an extensive new interferometric dataset in the mid-infrared in order to study the nuclear dust distribution in the Circinus galaxy. Due to our optimised observing strategy we could increase the uv coverage from 21 uv points to 152. This allows us to more precisely determine the properties of the dust distribution in the Circinus galaxy. Using both the correlated fluxes and the differential phases measured by the interferometer, we come to the following conclusions:

- We confirm the two-component structure previously found in the dust distribution of the Circinus galaxy, consisting of an inner dense disk-like component and an extended emission region. We interpret this as emission from warm dust in the context of an inner dense disk surrounded by a less dense, geometrically thick and filamentary dust distribution.
- The disk-like component is highly elongated with a size (FWHM) of ~ 0.2 pc \times 1.1 pc. Its major axis is along PA $\sim 46^\circ$, which is in perfect agreement to the orientation of the nuclear maser disk and oriented perpendicular to the ionisation cone and outflow along PA $\sim -44^\circ$. Because a flat, dense disk should appear in absorption rather than emission when seen close to edge-on, we interpret this component either as emission from material associated with the inner funnel of the torus directly above or below the disk or from the directly illuminated portion of a warped disk slightly oriented towards us.
- The extended dust emission is responsible for 80% of the mid-infrared emission. It has a FWHM of ~ 0.8 pc \times 1.9 pc and is elongated along PA $\sim 107^\circ$, that is, roughly in polar direction. We see this component as the inner part of the extended emission already seen by single dish imaging. It is interpreted as the emission from the inner funnel of a more extended dust distribution and especially as emission from the funnel edge along PA $\sim -90^\circ$. Dense dusty material enters the ionisation cone primarily on this side of the funnel, which is also preferentially illuminated by the inclined accretion disk.
- We detect significant differential phases, indicating both chromatic and spatial asymmetries in the dust emission. On scales of ~ 1.0 pc, the differential phases are well explained by a strong increase in the silicate absorption depth towards the south-east. This strong gradient in the silicate absorption implies that a significant amount of obscuration takes place on parsec scales. It also shows that the galaxy is more obscured towards the south-east all the way to the nucleus. The more complex differential phase signal on longer baselines is most likely caused by intermediate scale asymmetries in the brightness distribution, both chromatic and achromatic. These are probably not individual clumps of a clumpy torus, but rather intermediate scale structures such as the warp of the inner disk, the sharp cone edges or large filamentary structures which are directly illuminated by the central engine.
- We find no indications for a temperature difference in the dust distribution between ~ 0.1 pc to ~ 40 pc. On all of these scales, the mid-infrared spectrum has roughly the same

⁷ The dust directly illuminated by the central engine generally dominates the emission, see discussion in Sect. 5.1.

slope, indicative of dust at $T \sim 300$ K. Because the SED shows excess emission in the near-infrared with respect to emission by 300 K dust, we argue that this emission must also be extended on scales >0.3 pc. Otherwise, the Rayleigh-Jeans part of the compact hot dust component would appear as an unresolved source in our interferometric data in the mid-infrared. This is in contrast to the results for other well studied AGN such as NGC 1068 and NGC 424, where a clear temperature increase towards the centre is observed. This result also has a consequence for MATISSE (Lopez et al. 2008), the successor to MIDI at the VLTI: we predict relatively low visibilities also in the L and M -band for the Circinus galaxy.

- We further argue that the dense inner disk is not sufficient to provide the obscuration and collimation observed on larger scales, that is, the function normally attributed to the dusty torus in unified schemes of AGN. These must be caused by additional material above and below the disk on scales of ~ 1 pc. The emission from the polar component is substantially from the inner funnel of this dust distribution.

Our interferometric observations show a quite complex picture of the dust emission in the nucleus of the Circinus galaxy. To fully and unambiguously reveal the underlying brightness distribution, interferometric observations enabling image reconstruction will be necessary. Because MIDI is only a two beam interferometer, it measures no closure phases and a reliable image reconstruction is therefore not readily possible. This will, however, soon be possible with the upcoming second generation mid-infrared beam combiner for the VLTI, MATISSE, which will combine four telescopes at a time and thus provide three closure phases.

The presence of a bright disk-like component, polar elongated dust emission and the lack of a temperature difference are not expected for typical models of the centrally heated dust distributions of AGN. New sets of detailed radiative transfer calculations will be required to explain our observations and to better understand the three-dimensional dust morphology in the nuclei of active galaxies.

Acknowledgements. We thank the ESO staff operating the VLT(I) and the night astronomers on duty during our observations for their support. Without their assistance and help, it would not have been possible to collect this unique data set. We also thank D. Asmus and A. Kreplin for helpful discussions and their suggestions to improve the manuscript, as well as the anonymous referee for the detailed comments strengthening the manuscript. We are very grateful to K. Zelenevskiy for proof-reading the manuscript.

References

- Alexander, D. M., Heisler, C. A., Young, S., et al. 2000, *MNRAS*, **313**, 815
- Antonucci, R. 1993, *ARA&A*, **31**, 473
- Antonucci, R. R. J., & Miller, J. S. 1985, *ApJ*, **297**, 621
- Barvainis, R. 1987, *ApJ*, **320**, 537
- Beckert, T., Driebe, T., Hönl, S. F., & Weigelt, G. 2008, *A&A*, **486**, L17
- Bianchi, S., Maiolino, R., & Risaliti, G. 2012, *Adv. Astron.*, **2012**
- Bland-Hawthorn, J., Gallimore, J. F., Tacconi, L. J., et al. 1997, *Ap&SS*, **248**, 9
- Burtscher, L. 2011, Ph.D. Thesis, Max-Planck-Institut für Astronomie, Heidelberg, Germany
- Burtscher, L., Jaffe, W., Raban, D., et al. 2009, *ApJ*, **705**, L53
- Burtscher, L., Meisenheimer, K., Jaffe, W., Tristram, K. R. W., & Röttgering, H. J. A. 2010, *PASA*, **27**, 490
- Burtscher, L., Tristram, K. R. W., Jaffe, W. J., & Meisenheimer, K. 2012, in Proc. SPIE, **8445**, 84451G
- Burtscher, L., Meisenheimer, K., Tristram, K. R. W., et al. 2013, *A&A*, **558**, A149
- Curran, S. J., Johansson, L. E. B., Rydbeck, G., & Booth, R. S. 1998, *A&A*, **338**, 863
- Curran, S. J., Rydbeck, G., Johansson, L. E. B., & Booth, R. S. 1999, *A&A*, **344**, 767
- Deroo, P., van Winckel, H., Verhoelst, T., et al. 2007, *A&A*, **467**, 1093
- Dorodnitsyn, A., Kallman, T., & Proga, D. 2008, *ApJ*, **675**, L5
- Dullemond, C. P., Dominik, C., & Natta, A. 2001, *ApJ*, **560**, 957
- Efron, B. 1979, *Ann. Stat.*, **7**, 1
- Elmouttie, M., Haynes, R. F., Jones, K. L., Sadler, E. M., & Ehle, M. 1998, *MNRAS*, **297**, 1202
- Feltre, A., Hatziminaoglou, E., Fritz, J., & Franceschini, A. 2012, *MNRAS*, **426**, 120
- Fischer, T. C., Crenshaw, D. M., Kraemer, S. B., & Schmitt, H. R. 2013, *ApJS*, **209**, 1
- Freeman, K. C., Karlsson, B., Lynga, G., et al. 1977, *A&A*, **55**, 445
- Galliano, F., Madden, S. C., Tielens, A. G. G. M., Peeters, E., & Jones, A. P. 2008, *ApJ*, **679**, 310
- Gitton, P. B., Leveque, S. A., Avila, G., & Phan Duc, T. 2004, in New Frontiers in Stellar Interferometry, ed. W. A. Traub, Proc. SPIE, **5491**, 944
- Granato, G. L., & Danese, L. 1994, *MNRAS*, **268**, 235
- Greenhill, L. J., Booth, R. S., Ellingsen, S. P., et al. 2003, *ApJ*, **590**, 162
- Hagiwara, Y., Miyoshi, M., Doi, A., & Horiuchi, S. 2013, *ApJ*, **768**, L38
- Hall, P. 1985, *Stochastic Processes and their Applications*, **20**, 231
- Hönl, S. F., & Kishimoto, M. 2010, *A&A*, **523**, A27
- Hönl, S. F., Kishimoto, M., Antonucci, R., et al. 2012, *ApJ*, **755**, 149
- Hönl, S. F., Kishimoto, M., Tristram, K. R. W., et al. 2013, *ApJ*, **771**, 87
- Hopkins, P. F., Hayward, C. C., Narayanan, D., & Hernquist, L. 2012, *MNRAS*, **420**, 320
- Horst, H., Duschl, W. J., Gandhi, P., & Smette, A. 2009, *A&A*, **495**, 137
- Jaffe, W. J. 2004, in New Frontiers in Stellar Interferometry, ed. W. A. Traub, Proc. SPIE, **5491**, 715
- Jaffe, W., Meisenheimer, K., Röttgering, H. J. A., et al. 2004, *Nature*, **429**, 47
- Kemper, F., Vriend, W. J., & Tielens, A. G. G. M. 2004, *ApJ*, **609**, 826
- Kishimoto, M., Hönl, S. F., Tristram, K. R. W., & Weigelt, G. 2009a, *A&A*, **493**, L57
- Kishimoto, M., Hönl, S. F., Antonucci, R., et al. 2009b, *A&A*, **507**, L57
- Kishimoto, M., Hönl, S. F., Antonucci, R., et al. 2011a, *A&A*, **527**, A121
- Kishimoto, M., Hönl, S. F., Antonucci, R., et al. 2011b, *A&A*, **536**, A78
- Koribalski, B. S., Staveley-Smith, L., Kilborn, V. A., et al. 2004, *AJ*, **128**, 16
- Kreplin, A., Weigelt, G., Kraus, S., et al. 2013, *A&A*, **551**, A21
- Krolik, J. H., & Begelman, M. C. 1988, *ApJ*, **329**, 702
- Kylafis, N. D., & Norman, C. A. 1991, *ApJ*, **373**, 525
- Leinert, C., Graser, U., Przygodna, F., et al. 2003, *Ap&SS*, **286**, 73
- Lo, K. Y. 2005, *ARA&A*, **43**, 625
- Lopez, B., Antonelli, P., Wolf, S., et al. 2008, in Proc. SPIE, **7013**, 70132B
- López-Gonzaga, N., Jaffe, W., Burtscher, L., Tristram, K. R. W., & Meisenheimer, K. 2014, *A&A*, submitted [[arXiv:1401.3248](https://arxiv.org/abs/1401.3248)]
- Lumsden, S. L., Alexander, D. M., & Hough, J. H. 2004, *MNRAS*, **348**, 1451
- Maiolino, R., Alonso-Herrero, A., Anders, S., et al. 2000, *ApJ*, **531**, 219
- Marconi, A., Moorwood, A. F. M., Origlia, L., & Oliva, E. 1994, *The Messenger*, **78**, 20
- Markwardt, C. B. 2009, in Astronomical Data Analysis Software and Systems XVIII, eds. D. A. Bohlender, D. Durand, & P. Dowler, *ASP Conf. Ser.*, **411**, 251
- Matt, G., Fiore, F., Perola, G. C., et al. 1996, *MNRAS*, **281**, L69
- Meisenheimer, K., Tristram, K. R. W., Jaffe, W., et al. 2007, *A&A*, **471**, 453
- Meisner, J. A., Tubbs, R. N., & Jaffe, W. J. 2004, in New Frontiers in Stellar Interferometry, ed. W. A. Traub, Proc. SPIE, **5491**, 725
- Moorwood, A. F. M., Lutz, D., Oliva, E., et al. 1996, *A&A*, **315**, L109
- Mor, R., Netzer, H., & Elitzur, M. 2009, *ApJ*, **705**, 298
- Moshir, M., Kopan, G., Conrow, T., et al. 1990, in BAAS, **22**, 1325
- Natta, A., Prusti, T., Neri, R., et al. 2001, *A&A*, **371**, 186
- Nenkova, M., Ivezić, Ž., & Elitzur, M. 2002, *ApJ*, **570**, L9
- Netzer, H. 1987, *MNRAS*, **225**, 55
- Oliva, E., Salvati, M., Moorwood, A. F. M., & Marconi, A. 1994, *A&A*, **288**, 457
- Oliva, E., Marconi, A., Cimatti, A., & Alighieri, S. D. S. 1998, *A&A*, **329**, L21
- Packham, C., Radomski, J. T., Roche, P. F., et al. 2005, *ApJ*, **618**, L17
- Packham, C., Young, S., Fisher, S., et al. 2007, *ApJ*, **661**, L29
- Poncellet, A., Perrin, G., & Sol, H. 2006, *A&A*, **450**, 483
- Poncellet, A., Doucet, C., Perrin, G., Sol, H., & Lagage, P. O. 2007, *A&A*, **472**, 823
- Pott, J., Malkan, M. A., Elitzur, M., et al. 2010, *ApJ*, **715**, 736
- Prieto, M. A., Meisenheimer, K., Marco, O., et al. 2004, *ApJ*, **614**, 135
- Prieto, M. A., Reunanen, J., Tristram, K. R. W., et al. 2010, *MNRAS*, **402**, 724
- Raban, D., Heijligers, B., Röttgering, H., et al. 2008, *A&A*, **484**, 341
- Raban, D., Jaffe, W., Röttgering, H., Meisenheimer, K., & Tristram, K. R. W. 2009, *MNRAS*, **394**, 1325
- Radomski, J. T., Piña, R. K., Packham, C., et al. 2003, *ApJ*, **587**, 117

- Ramos Almeida, C., Levenson, N. A., Rodríguez Espinosa, J. M., et al. 2009, *ApJ*, **702**, 1127
- Rees, M. J., Silk, J. I., Werner, M. W., & Wickramasinghe, N. C. 1969, *Nature*, **223**, 788
- Reunanen, J., Prieto, M. A., & Siebenmorgen, R. 2010, *MNRAS*, **402**, 879
- Roche, P. F., Packham, C., Telesco, C. M., et al. 2006, *MNRAS*, **367**, 1689
- Schartmann, M., Meisenheimer, K., Camenzind, M., Wolf, S., & Henning, T. 2005, *A&A*, **437**, 861
- Schartmann, M., Meisenheimer, K., Camenzind, M., et al. 2008, *A&A*, **482**, 67
- Schartmann, M., Meisenheimer, K., Klahr, H., et al. 2009, *MNRAS*, **393**, 759
- Schmitt, H. R., Pauls, T. A., Tycner, C., et al. 2006, in *Advances in Stellar Interferometry*, eds. J. D. Monnier, M. Schöller, et al., *Proc. SPIE*, **6268**, 3B
- Schweitzer, M., Groves, B., Netzer, H., et al. 2008, *ApJ*, **679**, 101
- Siebenmorgen, R., & Efstathiou, A. 2001, *A&A*, **376**, L35
- Smith, C. H., Wright, C. M., Aitken, D. K., Roche, P. F., & Hough, J. H. 2000, *MNRAS*, **312**, 327
- Smith, D. A., & Wilson, A. S. 2001, *ApJ*, **557**, 180
- Smith, J. D. T., Draine, B. T., Dale, D. A., et al. 2007, *ApJ*, **656**, 770
- Soldi, S., Beckmann, V., Bassani, L., et al. 2005, *A&A*, **444**, 431
- Suganuma, M., Yoshii, Y., Kobayashi, Y., et al. 2006, *ApJ*, **639**, 46
- Swain, M., Vasisht, G., Akeson, R., et al. 2003, *ApJ*, **596**, L163
- Tristram, K. R. W. 2007, Ph.D. Thesis, Max-Planck-Institut für Astronomie, Heidelberg, Germany
- Tristram, K. R. W. 2013 [[arXiv:1312.3607](https://arxiv.org/abs/1312.3607)]
- Tristram, K. R. W., & Schartmann, M. 2011, *A&A*, **531**, A99
- Tristram, K. R. W., Meisenheimer, K., Jaffe, W., et al. 2007, *A&A*, **474**, 837
- Tristram, K. R. W., Raban, D., Meisenheimer, K., et al. 2009, *A&A*, **502**, 67
- Urry, C. M., & Padovani, P. 1995, *PASP*, **107**, 803
- van Boekel, R. J. H. M. 2004, Ph.D. Thesis, University of Amsterdam, The Netherlands
- Veilleux, S., & Bland-Hawthorn, J. 1997, *ApJ*, **479**, L105
- Verhoelst, T. 2005, Ph.D. Thesis, Institute of Astronomy, K.U. Leuven, Belgium
- Wada, K. 2012, *ApJ*, **758**, 66
- Wada, K., & Norman, C. A. 2002, *ApJ*, **566**, L21
- Wada, K., Papadopoulos, P. P., & Spaans, M. 2009, *ApJ*, **702**, 63
- Weigelt, G., Wittkowski, M., Balega, Y. Y., et al. 2004, *A&A*, **425**, 77
- Wilson, A. S., Shopbell, P. L., Simpson, C., et al. 2000, *AJ*, **120**, 1325
- Wittkowski, M., Kervella, P., Arsenault, R., et al. 2004, *A&A*, **418**, L39
- Yang, Y., Wilson, A. S., Matt, G., Terashima, Y., & Greenhill, L. J. 2009, *ApJ*, **691**, 131

Appendix A: Table and plots of all uv points

Table A.1 lists all measurements of the Circinus galaxy obtained with MIDI, that is all uv points. The columns are: (1) a running number of the measurement; (2) the date and time at the start of the fringe track, i.e. the interferometric observation; (3) modified Julian date, MJD; (4) telescope combination used for the observation; (5) projected baseline length; (6) position angle of the projected baseline; (7) adaptive optics system used, either STRAP or MACAO (“_T” indicates additional usage of the technical CCD); (8) usage of IRIS with: “n/a” – IRIS not available, “off” – IRIS not used for field stabilisation, “on” – IRIS used for field stabilisation, a number – IRIS used with the integration time specified in seconds (before 2011 no IRIS integration times were stored with the data); (9) mode of the interferometric observations with: “0OPD” – tracking with a scan length of $84.2\ \mu\text{m}$ at zero OPD, “OFF” – tracking with a scan length of $84.2\ \mu\text{m}$ at an offset of $40\ \mu\text{m}$, “SHRT” – tracking with a reduced scan length

of $53.0\ \mu\text{m}$ at an offset of $40\ \mu\text{m}$; (10) detector integration time of MIDI; (11) chopping frequency for the observations of the total flux spectra with the single dishes; (12) airmass; (13) seeing; (14) coherence time; (15) name of the calibrator star; (16) time of the calibrator observation; (17) correlated flux and its error at $12\ \mu\text{m}$, if the observation was successful and is used for the further analysis. Measurements were considered successful if a fringe signal was tracked and sufficient signal was detected (mostly equivalent to more than 1500 good frames used for the averaging). No entry in the chop frequency column indicates that no photometry was observed.

All dispersed correlated fluxes are shown in Fig. A.1, the differential phases are plotted in Fig. A.2. The data is plotted in blue, the correlated fluxes and differential phases of the model from fit 3 are plotted in red. As in Table A.1, the measurements are ordered by observing date and time. The numbering is also the same as in Table A.1, however unsuccessful measurements are not plotted.

Table A.1. List of interferometric measurements of the Circinus galaxy obtained with MIDI.

#	Date and time	MJD	Baseline	BL [m]	PA [°]	AO mode	IRIS	Track mode	DIT [ms]	f_{chop} [Hz]	AM	Seeing [arcsec]	τ_0 [ms]	Calibrator name	Calibrator obs. date	F_{cor} [Jy]
(1)	(2)	(3)	(4)	(5)	(6)	(7)	(8)	(9)	(10)	(11)	(12)	(13)	(14)	(15)	(16)	(17)
1	2004-02-12 06:55:11	53047.28832	U3-U2	43.5	-160.7	STRAP_T	n/a	OOPD	20	2.0	1.47	0.96	3.4	HD120404	07:36:34	0.72 ± 0.12
2	2004-02-12 07:06:46	53047.29637	U3-U2	43.4	-158.5	STRAP_T	n/a	OOPD	20	2.0	1.45	0.91	3.6	HD120404	07:36:34	0.93 ± 0.15
3	2004-06-03 05:50:45	53159.24358	U3-U2	29.2	-87.0	STRAP_T	n/a	OOPD	12	2.0	1.69	0.68	4.3	HD120404	06:42:24	1.06 ± 0.13
4	2004-06-03 07:58:04	53159.33199	U3-U2	20.7	-50.3	STRAP_T	n/a	OOPD	12	2.0	2.54	0.73	4.2	HD120404	06:42:24	2.30 ± 0.29
5	2005-02-21 05:25:00	53422.22569	U2-U4	87.4	35.7	MACAO_T	n/a	OOPD	12	-	1.62	0.77	3.1	HD107446	04:38:01	-
6	2005-03-01 04:06:04	53430.17088	U3-U4	49.3	44.6	MACAO_T	n/a	OOPD	12	2.0	1.81	0.75	2.9	HD120404	03:34:58	0.46 ± 0.04
7	2005-03-01 04:38:30	53430.19340	U3-U4	51.0	53.6	MACAO_T	n/a	OOPD	12	2.0	1.67	0.72	3.0	HD120404	05:12:31	0.55 ± 0.05
8	2005-03-01 04:49:21	53430.20094	U3-U4	51.6	56.6	MACAO_T	n/a	OOPD	12	-	1.63	0.71	3.0	HD120404	05:12:31	0.76 ± 0.05
9	2005-03-01 06:58:52	53430.29088	U3-U4	58.1	88.4	MACAO_T	n/a	OOPD	12	2.0	1.36	0.74	2.8	HD120404	07:28:53	1.15 ± 0.06
10	2005-03-01 09:21:08	53430.38968	U3-U4	62.0	120.0	MACAO_T	n/a	OOPD	12	2.0	1.35	0.64	3.2	HD120404	09:43:25	1.27 ± 0.06
11	2005-03-01 10:08:22	53430.42248	U3-U4	62.4	130.5	MACAO_T	n/a	OOPD	12	2.0	1.40	1.25	1.6	HD120404	09:43:25	1.04 ± 0.06
12	2005-04-18 03:29:53	53478.14575	U2-U4	89.2	60.8	MACAO_T	n/a	OOPD	20	2.0	1.38	0.67	4.9	HD120404	02:48:03	0.28 ± 0.04
13	2005-05-26 23:29:03	53516.97851	U2-U3	43.8	12.8	MACAO_T	n/a	SHRT	12	2.0	1.56	0.63	3.3	HD120404	22:57:46	1.57 ± 0.07
14	2005-05-26 23:43:07	53516.98828	U2-U3	43.7	15.5	MACAO_T	n/a	SHRT	12	2.0	1.52	0.54	3.9	HD120404	22:57:46	1.58 ± 0.07
15	2005-05-27 01:37:29	53517.06770	U2-U3	42.0	37.0	MACAO_T	n/a	SHRT	18	2.0	1.34	0.67	3.1	HD120404	02:02:11	0.59 ± 0.04
16	2005-05-27 04:07:02	53517.17155	U2-U3	36.8	65.3	MACAO_T	n/a	SHRT	18	2.0	1.37	0.75	2.8	HD120404	03:40:07	0.36 ± 0.04
17	2005-05-27 04:17:27	53517.17878	U2-U3	36.3	67.3	MACAO_T	n/a	SHRT	18	2.0	1.39	0.98	2.1	HD120404	03:40:07	0.44 ± 0.03
18	2005-05-27 04:28:22	53517.18637	U2-U3	35.8	69.4	MACAO_T	n/a	OOPD	18	2.0	1.40	1.05	2.0	HD120404	03:40:07	0.40 ± 0.03
19	2006-05-18 06:16:21	53873.26135	U2-U3	31.7	84.2	MACAO	off	OFF	18	2.0	1.56	1.50	2.1	HD120404	06:42:24	0.97 ± 0.18
20	2006-05-18 07:09:48	53873.29847	U2-U3	28.2	96.4	MACAO	off	OFF	18	2.0	1.75	0.98	3.3	HD120404	06:42:24	1.35 ± 0.25
21	2006-05-18 08:04:13	53873.33626	U2-U3	24.5	110.7	MACAO	off	OFF	18	2.0	2.05	0.59	5.5	HD120404	06:42:24	1.73 ± 0.32
22	2006-05-18 08:17:34	53873.34553	U2-U3	23.6	114.7	MACAO	off	OFF	18	-	2.14	0.67	4.9	HD120404	06:42:24	1.66 ± 0.31
23	2008-04-17 05:25:12	54573.22583	U1-U3	84.6	42.2	MACAO	off	OFF	18	1.3	1.32	2.83	0.7	HD120404	04:51:31	-
24	2008-04-17 05:45:55	54573.24022	U1-U3	83.0	45.8	MACAO	off	OFF	20	1.3	1.33	2.38	0.8	HD120404	06:07:47	-
25	2008-04-17 06:40:57	54573.27844	U1-U3	78.1	55.5	MACAO	off	OFF	20	1.3	1.37	1.97	1.0	HD120404	06:07:47	-
26	2008-04-17 06:56:00	54573.28889	U1-U3	76.6	58.2	MACAO	off	OFF	20	1.3	1.39	2.62	0.7	HD120404	06:07:47	-
27	2008-04-17 07:10:30	54573.29896	U1-U3	75.0	60.8	MACAO	off	OFF	20	1.3	1.41	2.76	0.7	HD120404	08:02:55	-
28	2008-04-18 01:36:40	54574.06713	U2-U4	87.2	33.9	MACAO	off	OFF	18	1.3	1.64	0.69	3.8	HD120404	02:01:13	-
29	2008-04-18 02:31:50	54574.10544	U2-U4	88.3	47.4	MACAO	off	OFF	18	1.3	1.48	0.86	3.1	HD120404	02:01:13	0.42 ± 0.10
30	2008-04-18 02:42:44	54574.11301	U2-U4	88.5	50.0	MACAO	off	OFF	18	1.3	1.46	1.02	2.1	HD120404	02:01:13	0.52 ± 0.10
31	2008-04-18 02:50:14	54574.11822	U2-U4	88.7	51.7	MACAO	off	OFF	18	1.3	1.44	1.10	2.0	HD120404	03:24:43	0.45 ± 0.09
32	2008-04-18 02:59:04	54574.12435	U2-U4	88.8	53.8	MACAO	off	OFF	18	1.3	1.43	-	2.5	HD120404	03:24:43	0.46 ± 0.09
33	2008-04-18 03:48:32	54574.15870	U2-U4	89.4	65.3	MACAO	off	OFF	18	0.5	1.36	0.75	2.9	HD120404	03:24:43	0.47 ± 0.09
34	2008-04-18 03:59:03	54574.16601	U2-U4	89.4	67.7	MACAO	off	OFF	18	1.3	1.35	0.94	2.4	HD120404	03:24:43	0.42 ± 0.08
35	2008-04-18 04:09:51	54574.17351	U2-U4	89.4	70.2	MACAO	off	OFF	18	1.3	1.34	0.84	2.6	HD120404	04:56:27	0.38 ± 0.07
36	2008-04-18 04:20:48	54574.18111	U2-U4	89.4	72.7	MACAO	off	OFF	18	1.3	1.33	-	2.5	HD120404	04:56:27	0.35 ± 0.07
37	2008-04-18 04:30:42	54574.18799	U2-U4	89.4	74.9	MACAO	off	OFF	18	1.3	1.33	0.80	2.8	HD120404	04:56:27	0.40 ± 0.08
38	2008-04-18 05:29:35	54574.22888	U2-U4	88.6	88.3	MACAO	off	OFF	18	1.3	1.32	0.88	2.6	HD120404	04:56:27	0.29 ± 0.05
39	2008-04-18 05:42:59	54574.23818	U2-U4	88.3	91.3	MACAO	off	OFF	18	1.3	1.33	0.84	2.7	HD120404	04:56:27	-
40	2008-04-18 06:00:45	54574.25052	U2-U4	87.7	95.4	MACAO	off	OFF	18	1.3	1.34	0.76	3.0	HD120404	04:56:27	0.29 ± 0.05
41	2008-04-18 06:11:01	54574.25765	U2-U4	87.4	97.8	MACAO	off	OFF	18	1.3	1.35	0.59	3.9	HD120404	07:14:21	0.34 ± 0.05
42	2008-04-18 06:28:17	54574.26964	U2-U4	86.8	101.8	MACAO	off	OFF	18	1.3	1.36	0.78	3.0	HD120404	07:14:21	0.46 ± 0.05
43	2008-04-18 06:39:22	54574.27734	U2-U4	86.3	104.4	MACAO	off	OFF	18	1.3	1.37	0.87	2.7	HD120404	07:14:21	0.50 ± 0.06
44	2008-04-18 06:50:19	54574.28494	U2-U4	85.9	106.9	MACAO	off	OFF	18	1.3	1.39	0.95	2.4	HD120404	07:14:21	0.58 ± 0.06
45	2008-04-18 07:37:26	54574.31766	U2-U4	83.6	118.3	MACAO	off	OFF	18	1.3	1.47	0.73	3.6	HD120404	07:14:21	1.15 ± 0.12
46	2008-04-18 07:47:46	54574.32484	U2-U4	83.1	120.9	MACAO	off	OFF	18	1.3	1.50	0.75	3.5	HD120404	07:14:21	1.24 ± 0.13
47	2008-04-18 07:57:55	54574.33189	U2-U4	82.6	123.4	MACAO	off	OFF	18	1.3	1.52	-	3.9	HD120404	07:14:21	1.27 ± 0.13
48	2008-04-18 08:08:12	54574.33903	U2-U4	82.0	126.0	MACAO	off	OFF	18	1.3	1.55	0.64	4.1	HD120404	07:14:21	1.38 ± 0.14
49	2008-04-18 08:18:52	54574.34644	U2-U4	81.5	128.8	MACAO	off	OFF	18	1.3	1.58	0.87	3.0	HD120404	07:14:21	1.30 ± 0.13
50	2008-04-18 08:28:48	54574.35333	U2-U4	80.9	131.3	MACAO	off	OFF	18	1.3	1.61	0.83	3.2	HD120404	07:14:21	1.12 ± 0.12
51	2008-04-18 09:15:46	54574.38595	U2-U4	78.6	143.9	MACAO	off	OFF	18	1.3	1.80	1.20	2.2	HD120404	08:51:35	1.42 ± 0.14
52	2008-04-18 09:25:56	54574.39301	U2-U4	78.2	146.7	MACAO	off	OFF	18	1.3	1.85	1.25	2.1	HD120404	08:51:35	0.99 ± 0.10
53	2008-04-18 09:36:06	54574.40007	U2-U4	77.7	149.5	MACAO	off	OFF	18	1.3	1.90	1.82	1.5	HD120404	08:51:35	0.63 ± 0.08
54	2008-04-18 09:50:46	54574.41025	U2-U4	77.2	153.6	MACAO	off	OFF	18	1.3	1.99	1.23	2.2	HD120404	08:51:35	0.58 ± 0.07
55	2008-04-18 10:01:09	54574.41747	U2-U4	76.8	156.6	MACAO	off	OFF	18	1.3	2.05	1.18	2.3	HD120404	08:51:35	0.66 ± 0.07
56	2008-04-26 00:11:26	54582.00794	E0-G0	15.9	14.8	STRAP	off	OFF	20	1.3	1.88	0.91	2.0	HD125687	23:30:59	7.62 ± 1.65
57	2008-04-26 00:23:42	54582.01646	E0-G0	15.9	17.7	STRAP	off	OFF	20	1.3	1.81	0.72	2.5	HD125687	23:30:59	7.50 ± 1.63
58	2008-04-26 00:35:58	54582.02498	E0-G0	15.9	20.6	STRAP	off	OFF	20	1.3	1.76	-	2.2	HD125687	23:30:59	7.76 ± 1.63
59	2008-04-26 00:55:33	54582.03858	E0-G0	15.9	25.3	STRAP	off	OFF	20	1.3	1.68	0.69	2.6	HD125687	02:15:06	7.49 ± 1.63
60	2008-04-26 01:09:14	54582.04808	E0-G0	16.0	28.5	STRAP	off	OFF	20	1.3	1.63	0.73	2.4	HD125687	02:15:06	9.12 ± 1.90
61	2008-04-26 01:22:53	54582.05756	E0-G0	16.0	31.7	STRAP	off	OFF	20	1.3	1.58	-	3.1	HD125687	02:15:06	8.36 ± 1.77
62	2008-04-26 02:55:34	54582.12192	E0-G0	16.0	52.9	STRAP	off	OFF	18	1.3	1.38	0.86	2.0	HD125687	02:15:06	7.03 ± 1.53
63	2008-04-26 03:09:22	54582.13150	E0-G0	16.0	56.0	STRAP	off	OFF	20	1.3	1.37	1.05	1.6	HD125687	02:15:06	5.79 ± 1.26
64	2008-04-26 03:23:02	54582.14100	E0-G0	15.9	59.0	STRAP	off	OFF	20	1.3	1.35	1.07	1.6	HD125687	02:15:06	7.44 ± 1.56
65	2008-04-26 03:36:44	54582.15051	E0-G0	15.9	62.1	STRAP	off	OFF	20	1.3	1.34	0.90	1.9	HD125687	02:15:06	7.28 ± 1.54
66	2008-04-26 03:50:35	54582.16013	E0-G0	1												

Table A.1. continued.

#	Date and time	MJD	Baseline	BL	PA	AO	IRIS	Track	DIT	f_{chop}	AM	Seeing	τ_0	Calibrator	Calibrator	F_{cor}
(1)	(2)	(3)	(4)	[m]	[$^{\circ}$]	mode	(8)	mode	[ms]	[Hz]	(12)	[arcsec]	[ms]	name	obs. date	[Jy]
70	2008-04-26 04:46:56	54582.19926	E0-G0	15.6	77.7	STRAP	off	OFF	20	1.3	1.32	0.65	2.6	HD125687	02:15:06	5.54 \pm 1.27
71	2008-04-26 05:39:55	54582.23605	E0-G0	15.2	89.6	STRAP	off	OFF	20	1.3	1.35	–	3.7	HD125687	07:30:43	3.80 \pm 0.85
72	2008-04-26 05:53:32	54582.24551	E0-G0	15.0	92.7	STRAP	off	OFF	20	1.3	1.36	0.56	2.9	HD125687	07:30:43	4.67 \pm 0.85
73	2008-04-26 06:07:07	54582.25494	E0-G0	14.9	95.8	STRAP	off	OFF	20	1.3	1.37	0.54	3.1	HD125687	07:30:43	4.21 \pm 0.79
74	2008-04-26 06:31:48	54582.27208	E0-G0	14.6	101.6	STRAP	off	OFF	20	1.3	1.41	0.46	3.6	HD125687	07:30:43	4.04 \pm 0.44
75	2008-04-26 06:45:29	54582.28159	E0-G0	14.4	104.9	STRAP	off	OFF	20	1.3	1.43	0.53	3.1	HD125687	07:30:43	4.17 \pm 0.46
76	2008-04-26 06:59:04	54582.29102	E0-G0	14.3	108.2	STRAP	off	OFF	20	1.3	1.46	0.50	3.3	HD125687	07:30:43	3.62 \pm 0.45
77	2008-04-26 08:13:10	54582.34248	E0-G0	13.3	127.2	STRAP	off	OFF	20	1.3	1.67	0.74	2.2	HD125687	07:30:43	5.55 \pm 0.48
78	2008-04-26 08:26:51	54582.35198	E0-G0	13.1	130.9	STRAP	off	OFF	20	1.3	1.72	0.89	1.8	HD125687	09:06:34	6.57 \pm 0.64
79	2008-04-26 08:40:23	54582.36138	E0-G0	13.0	134.7	STRAP	off	OFF	20	1.3	1.78	0.74	2.1	HD125687	09:06:34	5.91 \pm 0.63
80	2008-04-26 09:51:50	54582.41100	E0-G0	12.2	155.8	STRAP	off	OFF	20	1.3	2.22	0.65	2.4	HD125687	09:06:34	–
81	2009-04-15 02:22:06	54936.09868	U1-U3	92.2	8.4	MACAO	off	OFF	20	0.5	1.54	–	4.8	HD120404	04:33:39	–
82	2009-04-15 02:46:23	54936.11554	U1-U3	91.8	12.7	MACAO	on	OFF	20	0.5	1.48	1.10	6.6	HD120404	04:33:39	0.33 \pm 0.07
83	2009-04-15 05:16:40	54936.21991	U1-U3	85.8	39.2	MACAO	on	OFF	20	0.5	1.32	0.90	6.3	HD120404	04:33:39	0.44 \pm 0.05
84	2009-04-15 05:27:24	54936.22736	U1-U3	85.0	41.0	MACAO	on	OFF	20	0.5	1.32	0.89	6.0	HD120404	04:33:39	0.49 \pm 0.05
85	2009-04-15 05:40:18	54936.23632	U1-U3	84.1	43.3	MACAO	on	OFF	20	0.5	1.32	0.83	6.0	HD120404	06:32:46	0.58 \pm 0.06
86	2009-04-15 06:00:23	54936.25027	U1-U3	82.6	46.8	MACAO	on	OFF	20	0.5	1.33	0.73	7.1	HD120404	06:32:46	0.64 \pm 0.06
87	2009-04-15 06:11:44	54936.25815	U1-U3	81.6	48.8	MACAO	on	OFF	20	0.5	1.34	0.62	7.5	HD120404	06:32:46	0.61 \pm 0.06
88	2009-04-15 06:53:02	54936.28683	U1-U3	77.8	56.1	MACAO	on	OFF	20	0.5	1.38	0.71	6.4	HD120404	06:32:46	0.53 \pm 0.06
89	2009-04-15 07:05:15	54936.29531	U1-U3	76.5	58.3	MACAO	on	OFF	20	0.5	1.39	0.70	6.5	HD120404	06:32:46	0.48 \pm 0.05
90	2009-04-15 07:16:37	54936.30321	U1-U3	75.3	60.3	MACAO	on	OFF	20	0.5	1.41	0.70	7.1	HD120404	06:32:46	0.48 \pm 0.05
91	2009-04-15 07:31:40	54936.31366	U1-U3	73.6	63.0	MACAO	on	OFF	20	0.5	1.43	0.68	7.1	HD120404	08:24:43	0.51 \pm 0.05
92	2009-04-15 07:53:51	54936.32906	U1-U3	71.0	67.1	MACAO	on	OFF	20	0.5	1.48	0.58	7.9	HD120404	08:24:43	0.51 \pm 0.05
93	2009-04-15 08:05:12	54936.33694	U1-U3	69.5	69.2	MACAO	on	OFF	20	0.5	1.51	0.72	6.9	HD120404	08:24:43	0.55 \pm 0.05
94	2009-04-15 08:46:51	54936.36587	U1-U3	63.9	77.3	MACAO	on	OFF	20	0.5	1.63	0.57	9.8	HD120404	08:24:43	1.01 \pm 0.09
95	2009-04-15 08:57:49	54936.37348	U1-U3	62.3	79.5	MACAO	on	OFF	20	–	1.67	0.64	9.1	HD120404	08:24:43	1.21 \pm 0.11
96	2009-04-15 09:29:24	54936.39542	U1-U3	57.5	86.1	MACAO	on	OFF	20	0.5	1.80	0.45	15.1	HD120404	08:24:43	1.31 \pm 0.11
97	2009-04-15 09:38:31	54936.40175	U1-U3	56.1	88.1	MACAO	off	OFF	20	0.5	1.85	0.63	10.0	HD120404	08:24:43	1.39 \pm 0.12
98	2009-04-15 09:47:40	54936.40810	U1-U3	54.7	90.2	MACAO	off	OFF	20	0.5	1.89	0.46	14.1	HD120404	08:24:43	1.57 \pm 0.14
99	2009-04-27 00:15:00	54948.01042	E0-G0	15.9	16.3	STRAP	off	OFF	20	0.5	1.84	1.07	2.3	HD125687	01:03:58	6.06 \pm 0.94
100	2009-04-27 00:28:53	54948.02006	E0-G0	15.9	19.6	STRAP	off	OFF	20	0.5	1.78	0.98	2.5	HD125687	01:03:58	5.90 \pm 0.92
101	2009-04-27 00:42:38	54948.02961	E0-G0	15.9	22.9	STRAP	off	OFF	20	0.5	1.72	0.86	2.9	HD125687	01:03:58	6.41 \pm 0.99
102	2009-04-27 01:35:15	54948.06615	E0-G0	16.0	35.3	STRAP	off	OFF	20	0.5	1.54	1.24	1.9	HD125687	01:03:58	5.78 \pm 0.91
103	2009-04-27 01:48:49	54948.07557	E0-G0	16.0	38.4	STRAP	off	OFF	20	0.5	1.50	1.02	2.4	HD125687	01:03:58	6.66 \pm 1.04
104	2009-04-27 02:02:32	54948.08509	E0-G0	16.0	41.5	STRAP	off	OFF	20	0.5	1.47	0.72	3.3	HD125687	01:03:58	6.43 \pm 1.01
105	2009-04-27 02:38:40	54948.11019	E0-G0	16.0	49.8	STRAP	off	OFF	20	0.5	1.40	0.72	3.3	HD125687	03:16:15	6.42 \pm 0.98
106	2009-04-27 02:52:22	54948.11970	E0-G0	16.0	52.8	STRAP	off	OFF	20	0.5	1.38	0.71	3.3	HD125687	03:16:15	5.95 \pm 0.91
107	2009-04-27 03:46:34	54948.15734	E0-G0	15.9	64.9	STRAP	off	OFF	20	0.5	1.33	0.82	2.8	HD125687	03:16:15	5.22 \pm 0.82
108	2009-04-27 04:00:41	54948.16714	E0-G0	15.8	68.1	STRAP	off	OFF	20	0.5	1.33	1.21	1.9	HD125687	03:16:15	4.60 \pm 0.72
109	2009-04-27 04:14:15	54948.17656	E0-G0	15.7	71.1	STRAP	off	OFF	20	0.5	1.32	–	2.4	HD125687	03:16:15	4.20 \pm 0.67
110	2009-04-27 05:11:37	54948.21640	E0-G0	15.4	83.9	STRAP	off	OFF	20	0.5	1.33	1.89	1.2	HD125687	03:16:15	4.39 \pm 0.78
111	2009-04-27 05:25:19	54948.22591	E0-G0	15.3	86.9	STRAP	off	OFF	20	0.5	1.34	1.11	2.0	HD125687	03:16:15	4.56 \pm 0.80
112	2009-04-27 05:46:51	54948.24087	E0-G0	15.1	91.8	STRAP	off	OFF	20	0.5	1.35	1.12	2.0	HD125687	03:16:15	4.62 \pm 0.81
113	2009-04-27 06:00:25	54948.25029	E0-G0	14.9	95.0	STRAP	off	OFF	20	–	1.37	1.25	1.8	HD125687	03:16:15	–
114	2009-04-27 06:15:47	54948.26096	E0-G0	14.7	98.5	STRAP	off	OFF	20	0.5	1.39	1.23	1.9	HD125687	03:16:15	5.21 \pm 0.91
115	2009-04-27 07:16:50	54948.30336	E0-G0	14.0	113.3	STRAP	off	OFF	20	–	1.50	1.03	2.3	HD150798	06:51:20	3.78 \pm 0.94
116	2009-04-27 08:52:21	54948.36969	H0-G0	25.6	–41.1	STRAP	off	OFF	20	0.5	1.85	0.91	2.6	HD150798	08:16:24	–
117	2009-04-27 09:08:26	54948.38086	H0-G0	25.2	–36.4	STRAP	off	OFF	20	0.5	1.94	0.87	2.8	HD125687	09:48:32	2.54 \pm 0.80
118	2009-04-27 09:20:13	54948.38904	H0-G0	24.9	–32.9	STRAP	off	OFF	20	0.5	2.01	1.27	1.9	HD125687	09:48:32	3.32 \pm 0.68
119	2009-04-27 10:17:10	54948.42859	H0-G0	24.1	–15.4	STRAP	off	OFF	20	–	2.47	1.23	2.0	HD150798	10:28:55	2.64 \pm 0.80
120	2011-04-14 08:44:53	55665.36450	U1-U2	35.3	65.7	MACAO	2.0	OFF	18	0.5	1.60	1.46	1.6	HD120404	08:20:24	0.47 \pm 0.08
121	2011-04-17 00:24:53	55668.01728	U3-U4	47.6	33.4	MACAO	2.0	OFF	18	–	2.02	1.33	1.7	HD120404	00:04:07	0.47 \pm 0.04
122	2011-04-17 00:28:29	55668.01978	U3-U4	47.7	34.5	MACAO	2.0	OFF	18	–	2.00	1.41	1.6	HD120404	00:04:07	0.44 \pm 0.04
123	2011-04-17 00:32:00	55668.02222	U3-U4	47.9	35.5	MACAO	2.0	OFF	18	–	1.98	1.15	1.9	HD120404	00:04:07	0.37 \pm 0.04
124	2011-04-17 00:41:54	55668.02910	U3-U4	48.3	38.5	MACAO	2.0	OFF	18	–	1.92	1.30	1.7	HD120404	01:35:04	0.48 \pm 0.03
125	2011-04-17 00:45:38	55668.03169	U3-U4	48.5	39.6	MACAO	2.0	OFF	18	–	1.90	1.45	1.5	HD120404	01:35:04	0.49 \pm 0.03
126	2011-04-17 00:54:28	55668.03782	U3-U4	48.9	42.2	MACAO	1.0	OFF	18	–	1.85	2.15	1.0	HD120404	01:35:04	0.61 \pm 0.03
127	2011-04-17 01:04:39	55668.04490	U3-U4	49.4	45.1	MACAO	off	OFF	18	–	1.80	1.06	2.1	HD120404	01:35:04	0.72 \pm 0.04
128	2011-04-17 01:11:31	55668.04966	U3-U4	49.7	47.0	MACAO	0.5	OFF	18	–	1.77	1.06	2.1	HD120404	01:35:04	0.79 \pm 0.04
129	2011-04-17 01:18:06	55668.05424	U3-U4	50.1	48.9	MACAO	0.5	OFF	18	–	1.74	1.27	1.7	HD120404	01:35:04	0.81 \pm 0.06
130	2011-04-17 06:40:15	55668.27795	U3-U4	62.2	124.9	MACAO	0.5	OFF	18	1.5	1.37	1.04	1.9	HD120404	07:10:37	1.87 \pm 0.11
131	2011-04-18 01:34:01	55669.06529	U2-U4	87.1	32.6	MACAO	0.5	OFF	18	1.5	1.66	1.09	1.9	HD120404	02:19:54	0.25 \pm 0.03
132	2011-04-18 01:42:24	55669.07111	U2-U4	87.3	34.7	MACAO	0.5	OFF	18	1.5 ^a	1.63	1.18	1.8	HD120404	02:19:54	–

Notes. ^(a) Chopping during the interferometric observations.

Table A.1. continued.

#	Date and time	MJD	Baseline	BL	PA	AO	IRIS	Track	DIT	f_{chop}	AM	Seeing	τ_0	Calibrator	Calibrator	F_{cor}
(1)	(2)	(3)	(4)	[m]	[°]	mode		mode	[ms]	[Hz]		[arcsec]	[ms]	name	obs. date	[Jy]
				(5)	(6)	(7)	(8)	(9)	(10)	(11)	(12)	(13)	(14)	(15)	(16)	(17)
133	2011-04-18 01:45:59	55669.07360	U2-U4	87.4	35.6	MACAO	0.5	OFF	18	–	1.62	0.96	2.2	HD120404	02:19:54	0.23 ± 0.03
134	2011-04-18 01:49:36	55669.07611	U2-U4	87.4	36.4	MACAO	0.5	OFF	18	–	1.61	0.90	2.3	HD120404	02:19:54	0.25 ± 0.03
135	2011-04-18 01:53:06	55669.07854	U2-U4	87.5	37.3	MACAO	0.5	OFF	18	–	1.60	0.99	2.1	HD120404	02:19:54	0.25 ± 0.03
136	2011-04-18 01:56:35	55669.08096	U2-U4	87.6	38.1	MACAO	0.5	OFF	18	–	1.59	1.03	2.0	HD120404	02:19:54	0.30 ± 0.03
137	2011-04-18 02:00:18	55669.08354	U2-U4	87.6	39.1	MACAO	0.5	OFF	18	1.5	1.58	0.99	2.1	HD120404	02:19:54	0.31 ± 0.03
138	2011-04-18 02:09:09	55669.08969	U2-U4	87.8	41.2	MACAO	0.5	OFF	18	–	1.55	0.93	2.3	HD120404	02:19:54	0.35 ± 0.04
139	2011-04-19 04:43:38	55670.19697	U1-U3	86.9	35.8	MACAO	0.2	OFF	18	1.5	1.32	0.44	5.0	HD120404	05:21:06	0.35 ± 0.04
140	2011-04-19 04:55:06	55670.20493	U1-U3	86.2	37.8	MACAO	0.2	OFF	18	1.5	1.32	0.39	5.5	HD120404	05:21:06	0.40 ± 0.04
141	2011-04-20 08:09:26	55671.33988	U2-U4	81.7	127.6	MACAO	2.0	OFF	18	–	1.57	0.65	3.1	HD120404	07:58:44	1.69 ± 0.07
142	2011-04-20 08:13:05	55671.34242	U2-U4	81.5	128.6	MACAO	2.0	OFF	18	–	1.58	0.58	3.5	HD120404	07:58:44	1.79 ± 0.07
143	2011-04-20 08:16:35	55671.34485	U2-U4	81.3	129.5	MACAO	2.0	OFF	18	–	1.59	0.69	2.9	HD120404	07:58:44	1.78 ± 0.07
144	2011-04-20 08:21:05	55671.34797	U2-U4	81.1	130.6	MACAO	2.0	OFF	18	–	1.60	0.68	3.0	HD120404	07:58:44	1.74 ± 0.07
145	2011-04-20 08:25:22	55671.35095	U2-U4	80.9	131.7	MACAO	2.0	OFF	18	–	1.62	0.66	3.1	HD120404	07:58:44	1.77 ± 0.07
146	2011-04-20 08:28:50	55671.35336	U2-U4	80.7	132.6	MACAO	2.0	OFF	18	–	1.63	0.68	3.0	HD120404	07:58:44	1.76 ± 0.07
147	2011-04-20 08:32:21	55671.35580	U2-U4	80.5	133.6	MACAO	2.0	OFF	18	1.5	1.64	0.69	2.9	HD120404	09:06:50	1.92 ± 0.17
148	2011-04-20 08:41:06	55671.36188	U2-U4	80.0	135.9	MACAO	2.0	OFF	18	–	1.67	0.64	3.2	HD120404	09:06:50	1.84 ± 0.07
149	2011-04-20 08:44:37	55671.36432	U2-U4	79.9	136.8	MACAO	2.0	OFF	18	–	1.68	0.65	3.1	HD120404	09:06:50	1.78 ± 0.08
150	2011-04-20 08:48:07	55671.36675	U2-U4	79.7	137.8	MACAO	2.0	OFF	18	–	1.70	0.65	3.1	HD120404	09:06:50	1.85 ± 0.07
151	2011-04-20 08:51:34	55671.36914	U2-U4	79.5	138.7	MACAO	2.0	OFF	18	–	1.71	0.62	3.2	HD120404	09:06:50	1.82 ± 0.07
152	2011-04-20 08:54:59	55671.37152	U2-U4	79.4	139.6	MACAO	2.0	OFF	18	–	1.73	0.66	3.1	HD120404	09:06:50	1.71 ± 0.07
153	2011-04-20 09:24:00	55671.39167	U2-U4	78.0	147.5	MACAO	1.9	OFF	18	–	1.86	0.53	3.9	HD120404	09:06:50	1.27 ± 0.05
154	2011-04-20 09:28:50	55671.39502	U2-U4	77.8	148.9	MACAO	1.9	OFF	18	–	1.89	0.61	3.3	HD120404	09:45:13	1.11 ± 0.05
155	2011-04-20 09:32:20	55671.39745	U2-U4	77.7	149.8	MACAO	1.9	OFF	18	–	1.91	0.60	3.4	HD120404	09:45:13	0.94 ± 0.05
156	2011-04-20 09:35:53	55671.39992	U2-U4	77.5	150.8	MACAO	1.9	OFF	18	–	1.93	0.57	3.5	HD120404	09:45:13	0.89 ± 0.04
157	2011-05-06 00:25:36	55687.01778	C1-A1	15.9	–153.2	STRAP	off	OFF	18	–	1.65	1.34	1.8	HD125687	00:51:21	7.52 ± 1.47
158	2011-05-06 00:30:49	55687.02140	C1-A1	15.9	–152.0	STRAP	off	OFF	18	1.7	1.64	1.00	2.4	HD125687	00:51:21	6.31 ± 1.27
159	2011-05-06 01:42:07	55687.07091	C1-A1	16.0	–135.5	STRAP	off	OFF	18	1.7	1.45	0.91	2.7	HD125687	00:51:21	7.29 ± 1.44
160	2011-05-06 01:54:00	55687.07917	C1-A1	16.0	–132.8	STRAP	off	OFF	18	1.7	1.42	1.09	2.3	HD125687	00:51:21	6.93 ± 1.34
161	2011-05-06 02:09:35	55687.08999	C1-A1	16.0	–129.3	STRAP	off	OFF	18	–	1.40	0.91	2.7	HD125687	03:06:08	–
162	2011-05-06 02:39:33	55687.11080	C1-A1	15.9	–122.5	STRAP	off	OFF	18	1.7	1.36	1.11	2.3	HD125687	03:06:08	5.49 ± 1.04
163	2011-05-06 02:48:35	55687.11707	C1-A1	15.9	–120.5	STRAP	off	OFF	18	1.7	1.35	1.18	2.1	HD125687	03:06:08	5.12 ± 0.50
164	2011-05-06 04:12:56	55687.17565	D0-B2	27.2	–145.1	STRAP	off	OFF	18	–	1.32	1.18	2.2	HD125687	03:41:45	–
165	2011-05-06 04:35:55	55687.19161	D0-B2	26.7	–141.4	STRAP	off	OFF	18	–	1.33	–	2.5	HD125687	03:41:45	–
166	2011-05-06 05:48:14	55687.24183	C1-A1	14.7	–80.1	STRAP	off	OFF	18	1.7	1.40	1.62	1.7	HD125687	06:21:19	3.91 ± 1.53
167	2011-05-06 06:00:04	55687.25005	C1-A1	14.5	–77.3	STRAP	off	OFF	18	–	1.41	1.38	1.8	HD125687	06:21:19	3.93 ± 1.49
168	2011-05-06 06:03:41	55687.25256	C1-A1	14.5	–76.4	STRAP	off	OFF	18	–	1.42	1.39	1.7	HD125687	06:21:19	3.98 ± 1.65
169	2011-05-06 06:07:33	55687.25524	C1-A1	14.4	–75.5	STRAP	off	OFF	18	1.7	1.43	1.23	2.1	HD125687	06:21:19	4.82 ± 2.09

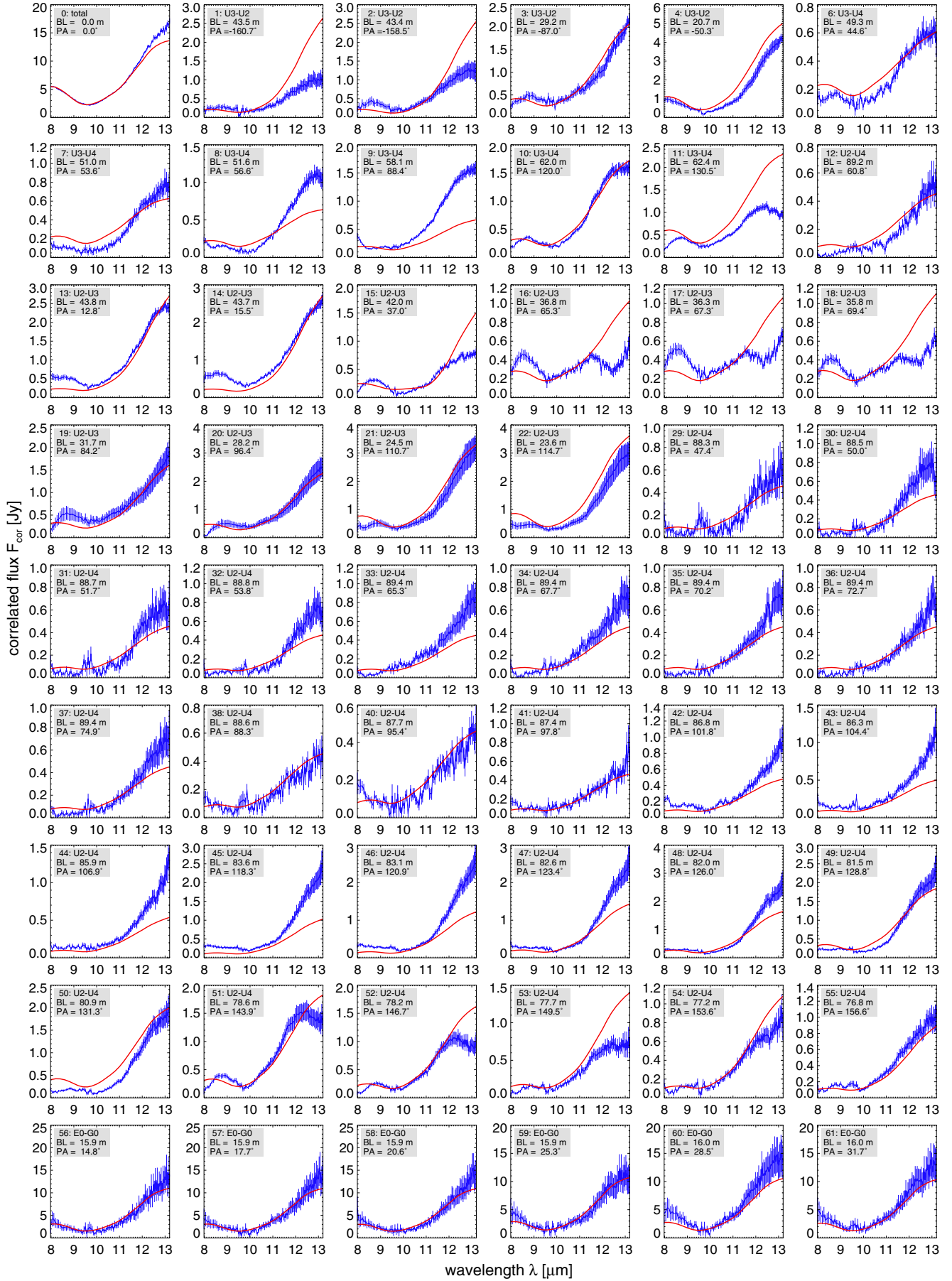


Fig. A.1. Correlated fluxes of all uw points (blue). The correlated fluxes of our three-component model (fit 3) are plotted in red.

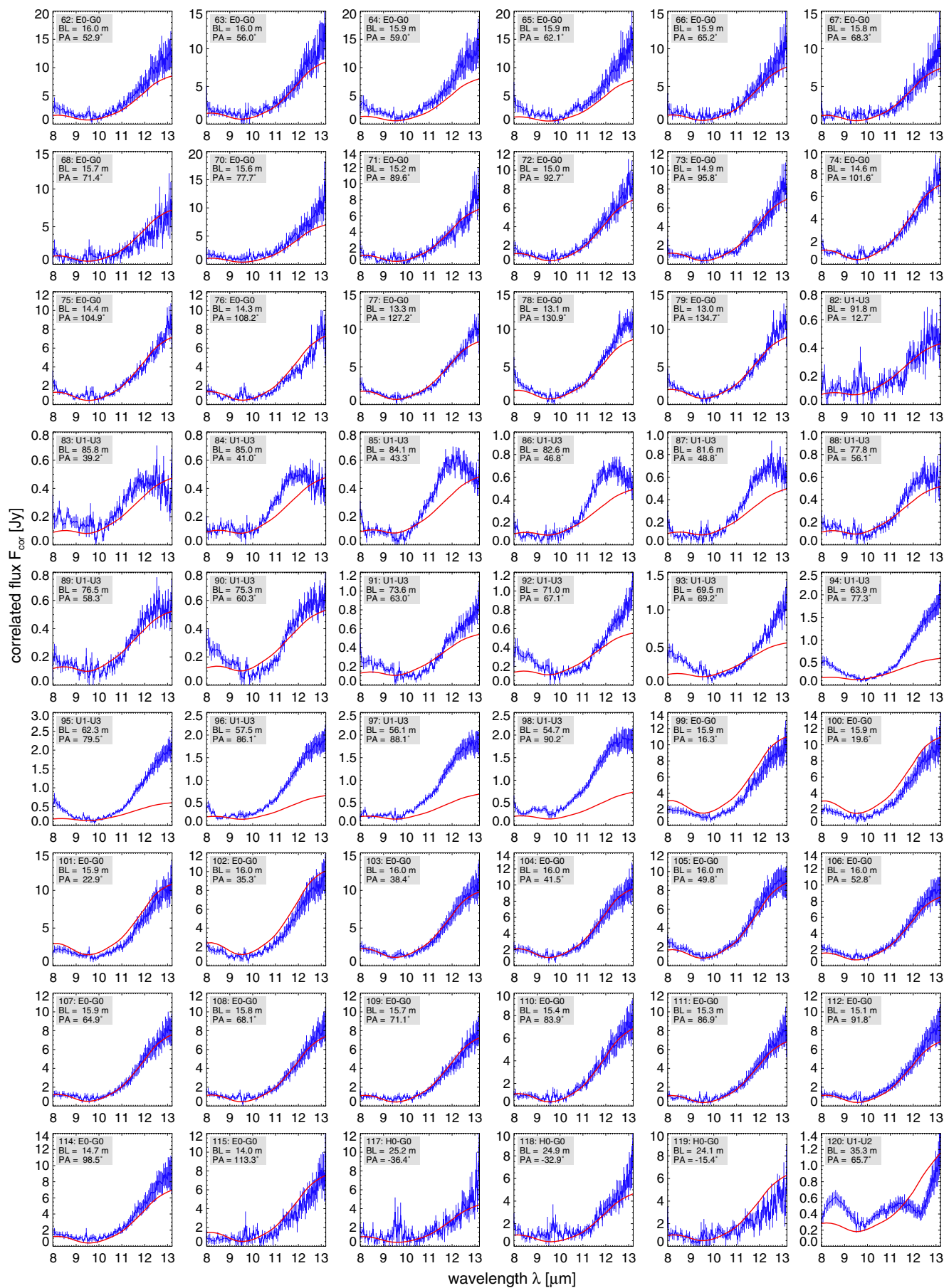


Fig. A.1. continued.

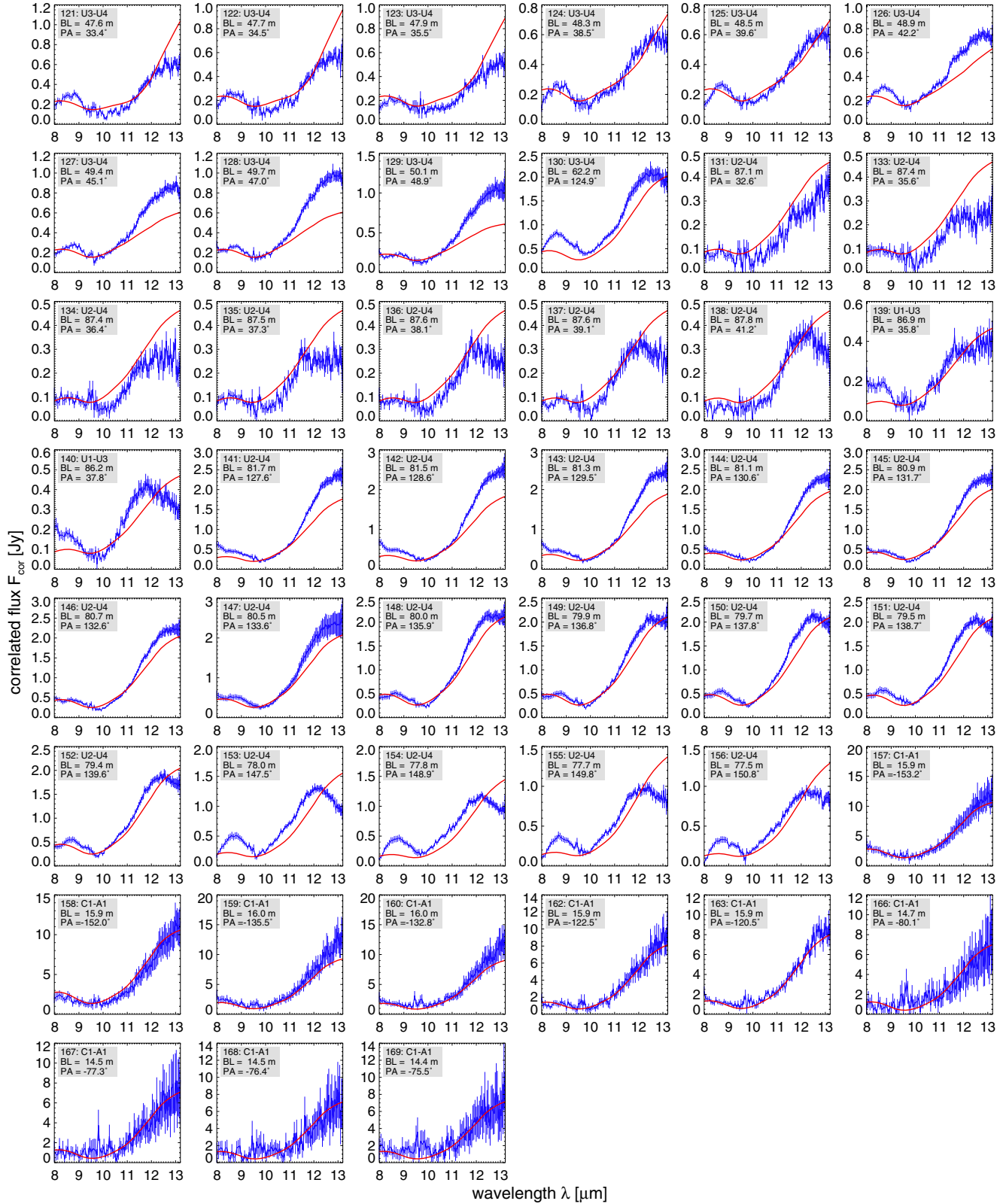


Fig. A.1. continued.

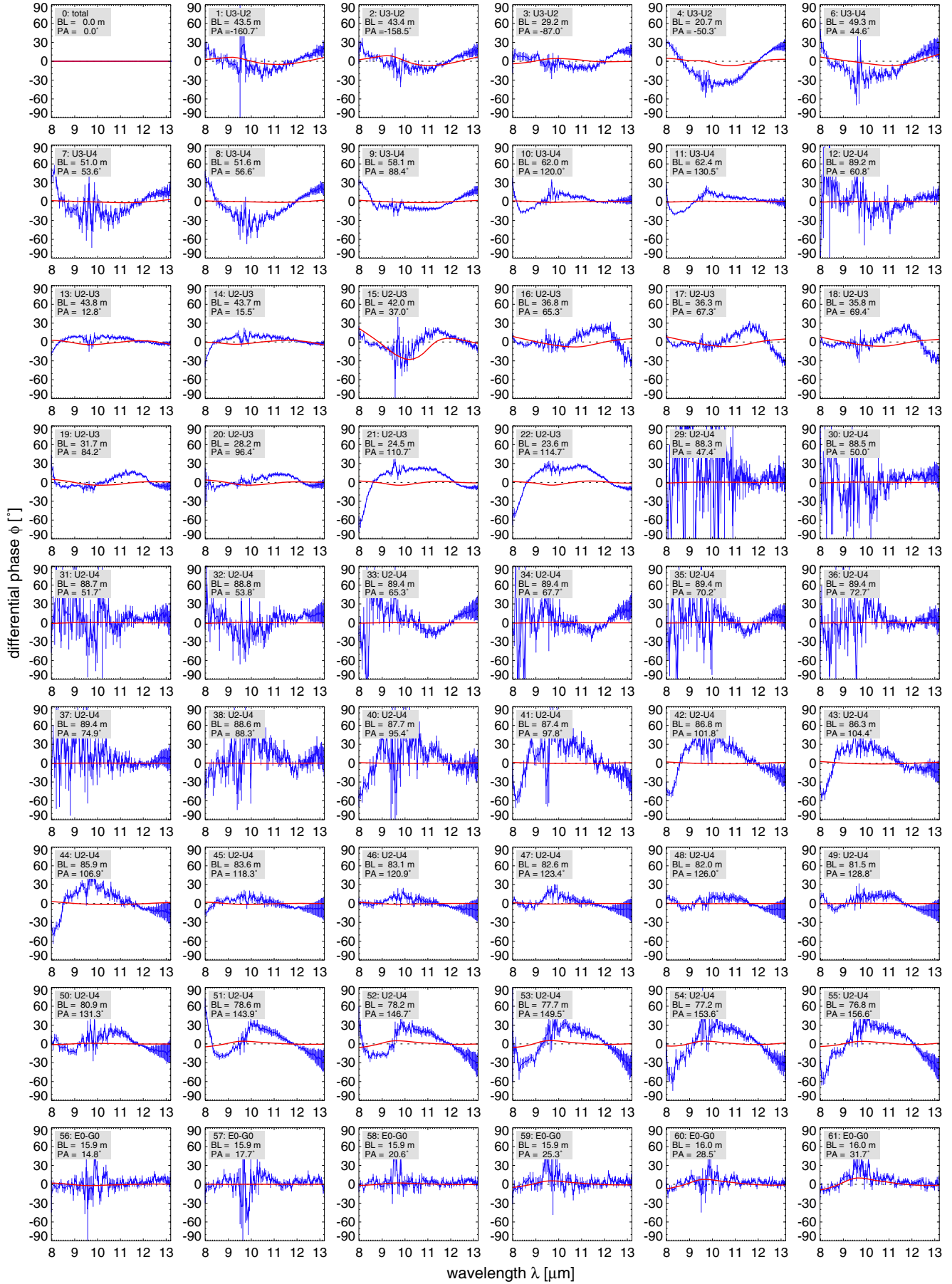


Fig. A.2. Differential phases of all w points (blue). The differential phases of our model (fit 3) are plotted in red.

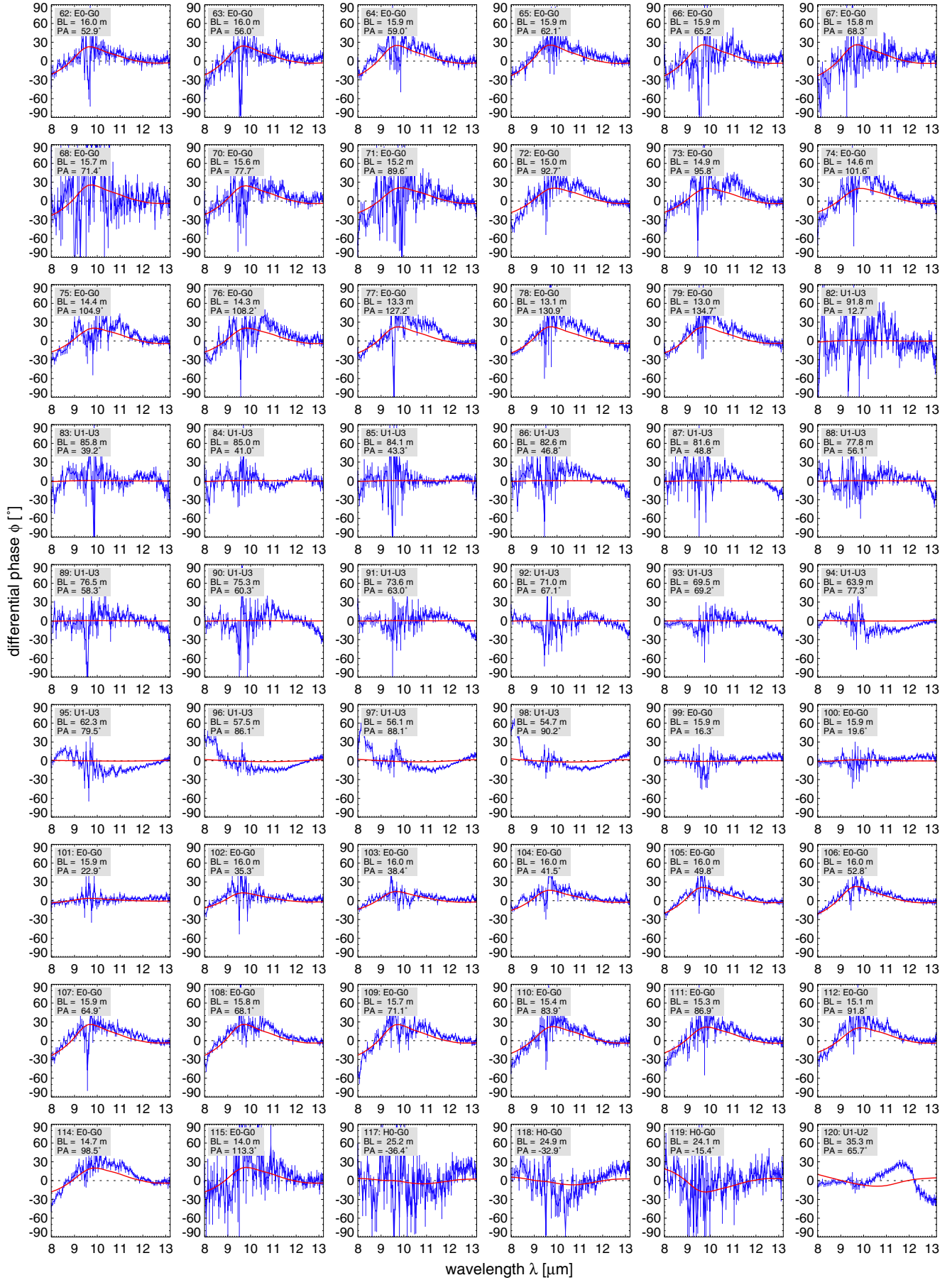


Fig. A.2. continued.

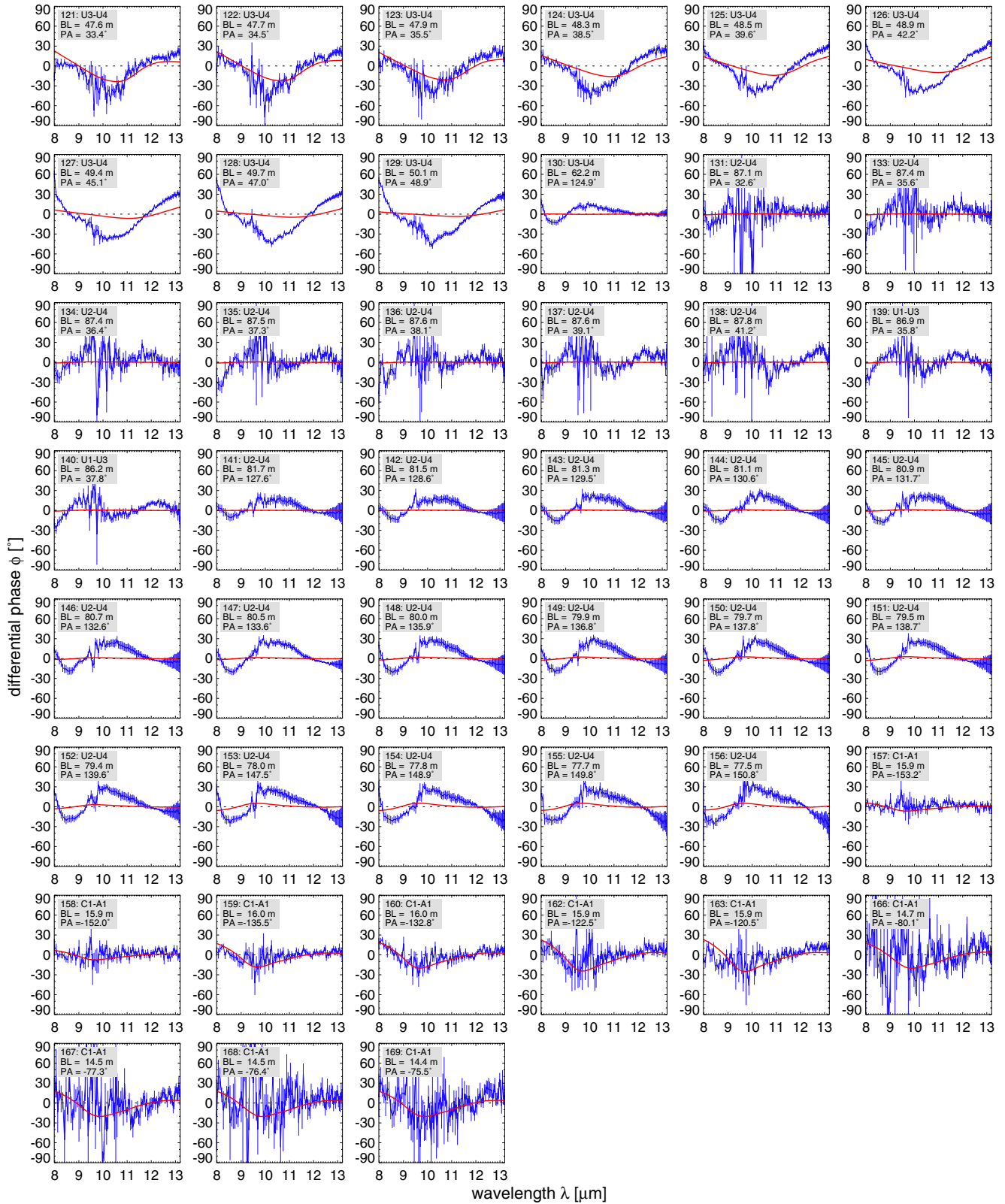


Fig. A.2. continued.